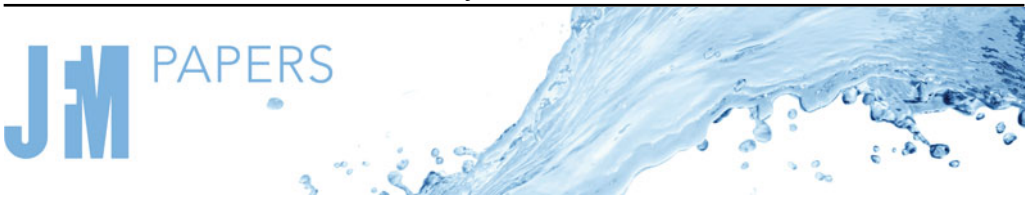
J. Fluid Mech. (2026), *vol.* 1027, A40, doi:10.1017/jfm.2025.11092



A hyperbolic description of mixing

Daniel Domínguez-Vázquez[1] **and Tomás Aquino**[1]

[1]Spanish National Research Council (IDAEA – CSIC), 08034 Barcelona, Spain

Corresponding author: Daniel Domínguez-Vázquez, daniel.dominguez@csic.es

(Received 10 June 2025; revised 2 December 2025; accepted 15 December 2025)

We introduce a description of passive scalar transport based on a (deterministic and hyperbolic) Liouville master equation. Defining a noise term based on time-independent random coefficients, instead of time-dependent stochastic processes, we circumvent the use of stochastic calculus to capture the one-point space–time statistics of solute particles in Lagrangian form deterministically. To find the proper noise term, we solve a closure problem for the first two moments locally in a streamline coordinate system, such that averaging the Liouville equation over the coefficients leads to the Fokker–Planck equation of solute particle locations. This description can be used to trace solute plumes of arbitrary shape, for any Péclet number, and in arbitrarily defined grids, thanks to the time reversibility of hyperbolic systems. In addition to grid flexibility, this approach offers some computational advantages as compared with particle tracking algorithms and grid-based partial differential equation solvers, including reduced computational cost, no Monte-Carlo-type sampling and unconditional stability. We reproduce known analytical results for the case of simple shear flow and extend the description of mixing in a vortex model to consider diffusion radially and nonlinearities in the flow, which govern the long time decay of the maximum concentration. Finally, we validate our formulation by comparing it with Monte Carlo particle tracking simulations in a heterogeneous flow field at the Darcy (continuum) scale.

Key words: dispersion, coupled diffusion and flow, computational methods

1. Introduction

Mixing is a fundamental process in fluid dynamics with strong implications for a wide range of disciplines, from combustion and atmospheric transport to biological flows and subsurface hydrology (Ottino 1990). It describes the phenomena governing the evolution

© The Author(s), 2026. Published by Cambridge University Press. This is an Open Access article, distributed under the terms of the Creative Commons Attribution licence (https://creativecommons.org/licenses/by/4.0/), which permits unrestricted re-use, distribution and reproduction, provided the original article is properly cited.

https://doi.org/10.1017/jfm.2025.11092 Published online by Cambridge University Press

of species from a more heterogeneous to a more homogeneous state via a combination of advection and diffusion (Dimotakis 2005; Villermaux 2019). Mixing is particularly important because its efficiency can dictate the rates of chemical reactions, heat transfer and material dispersion, ultimately controlling large-scale phenomena such as pollutant spreading (Egan & Mahoney 1972; Demuren & Rodi 1986), metabolic processes (Károlyi *et al.* 2002) and energy release in turbulent flames (Pope 1987).

While turbulent mixing has received much attention, laminar, time-independent flows in complex media can also lead to rich mixing dynamics that are not yet fully understood. A prominent example is flow through geological media, where the complexity of the mixing process arises from the presence of multiscale heterogeneity from the pore scale to the Darcy (continuum) scale (Dentz *et al.* 2011). In groundwater flows, long transport times and heterogeneous velocity fields create complex mixing dynamics, where solute stretching, diffusion and aggregation influence biogeochemical reaction rates (Monson & Kopelman 2000; Wright, Richter & Bolster 2017). Accurately capturing these mechanisms is crucial for predicting pollutant fate and assessing the effectiveness of remediation strategies in geophysical and environmental systems (Tartakovsky, Tartakovsky & Scheibe 2009; Tartakovsky 2013; Valocchi, Bolster & Werth 2019). At the pore scale, fluid deformation stretches and folds solute plumes, enhancing local concentration gradients and, therefore, the local action of diffusion, speeding up mixing (Le Borgne, Dentz & Villermaux 2015). Stationary, laminar flow at the pore scale can even lead to chaotic mixing, a phenomenon characterised by exponential stretching that is conjectured to be the norm in three-dimensional systems (Lester, Metcalfe & Trefry 2013; Turuban *et al.* 2018, 2019; Heyman *et al.* 2020; Aquino, Le Borgne & Heyman 2023). The relationship between pore-scale properties and continuum-scale mixing, dispersion and reaction remains an active topic of research (Puyguiraud *et al.* 2020; Lester *et al.* 2021, 2022; Dentz *et al.* 2018). The aim of the present work is to provide a new framework and corresponding numerical methodology to compute concentration plumes that accurately resolves mixing in this type of flow. The background flow is assumed to be known deterministically. In other words, even if the flow field is obtained from a stochastic description, the framework proposed here applies separately to given realisations. As such, we do not address incomplete knowledge directly, but we also do not require ergodicity or other averaging considerations (Dagan 1984; Balkovsky & Fouxon 1999; Dentz & de Barros 2015).

Two classical perspectives, Eulerian and Lagrangian, are commonly used to theoretically model and numerically simulate mixing phenomena. The former picture revolves around a deterministic partial differential equation (PDE) for the evolution of solute concentrations, namely the advection–dispersion equation (ADE). The Lagrangian picture is in turn typically based on the use of Langevin dynamics, i.e. stochastic differential equations to model the non-deterministic motion of solute particles (Pope 1985; Kinzelbach & Uffink 1991; Salamon, Fernàndez-Garcia & Gómez-Hernández 2006). The two pictures are reconciled through the fact that the concentration field normalised to unit mass may be seen as a probability density function (PDF) of solute particle positions, which solves a Fokker–Planck equation (FPE) equivalent to the ADE (Risken 1996). Each methodology is associated with certain benefits and difficulties. For example, grid-based Eulerian methods for solving the ADE become increasingly unstable and computationally demanding as the Péclet number increases, requiring regularisation techniques and filtering (Lv & Ihme 2014; Pirozzoli, Bernardini & Orlandi 2016; Shu 2020). In contrast to Eulerian descriptions, the Lagrangian approach avoids numerical dispersion and spurious mixing, capturing local concentration fluctuations and complex plume structure more accurately in heterogeneous flows (Benson *et al.* 2017). By tracking solute particles, this approach targets regions of the domain where the solute is present,

https://doi.org/10.1017/jfm.2025.11092 Published online by Cambridge University Press

saving computational effort when tracking complex but localised fronts (Salamon *et al.* 2006). However, other issues arise, such as sampling errors: as a rule of thumb, due to the central limit theorem, sampling errors lead to a slow Monte Carlo convergence $\sim N^{-1/2}$ with the number of particles N. While this is often not a practical issue when computing low-order moments, determining higher-order moments or the full concentration field to acceptable accuracy typically requires large numbers of particles, increasing the computational effort. Since these methods do not rely on the direct computation of local concentration values, an ancillary procedure is needed to reconstruct the PDF of solute particles, such as the use of kernel density estimators (Fernàndez-Garcia & Sánchez-Vila 2011; Pedretti & Fernàndez-Garcia 2013; Sole-Mari *et al.* 2019; Benson *et al.* 2021). Additionally, the use of high-order stochastic time integrators (Kloeden & Platen 1992) is not widespread, and while possible, in practice most studies rely on the Euler–Maruyama method (Maruyama 1955), which is of order $\Delta t^{1/2}$. Other difficulties relate to the determination of convergence rates and Courant–Friedrichs–Lewy-like criteria, because tracking particle positions essentially leads to a dynamic grid with nodes at locations that are not known *a priori*. Enforcing complex boundary conditions also presents challenges (Paster, Bolster & Benson 2014; Aquino 2024). New alternatives to tackle some of these challenges explore the use of graphics processing units (GPU)-accelerated particle tracking algorithms (Rizzo, Nakano & de Barros 2019) combined with models for PDF reconstruction (Bonazzi *et al.* 2023*a*).

An approach that combines characteristics of both the (deterministic) Eulerian and (stochastic) Lagrangian perspectives may be desirable from a methodological point of view and theoretical standpoint. Originally introduced in the context of turbulent mixing (Ranz 1979) and later adapted to confined flows through porous media (Villermaux 2019), the lamella model has been used to develop numerical algorithms that can track transported scalars deterministically but in a Lagrangian picture (Meunier & Villermaux 2010; Martínez-Ruiz *et al.* 2018; Sen *et al.* 2020; Meunier & Villermaux 2022; Pushenko *et al.* 2025). Mixing leads to the formation of elongated structures, called lamellae, that locally align with the principal direction of strain. Under certain approximations, these structures can be described with a canonical diffusion equation along the compression direction upon a suitable change of variables (Ranz 1979; Villermaux 2019; Dentz, Hidalgo & Lester 2023). However, computing plume evolution for non-uniform initial concentration profiles (Bonazzi *et al.* 2023*b*), at moderate to low Péclet numbers (Dentz *et al.* 2018), and for long times, when these structures coalesce (Heyman *et al.* 2024), remains difficult.

The main goal of the present paper is to introduce a hyperbolic description of mixing that allows for the theoretical and numerical treatment of passive scalar transport in a Lagrangian but deterministic form. The formulation is based on a high-dimensional Liouville master equation for the joint PDF of support particles. These are characterised by time-independent values of random coefficients and follow time-differentiable trajectories with the same one-point statistics as the solute particles. We impose that averaging the Liouville equation over the random coefficients must lead to the FPE, resulting in a classical moment closure problem. Adopting a local linearisation of the flow field described along a streamline coordinate system (Winter 1982; Dentz *et al.* 2016, 2018), and using a closure based on truncated central moments, we find conditions to determine the noise term, extending recent hyperbolic descriptions of elementary stochastic processes (Domínguez-Vázquez *et al.* 2024*b*). In order to avoid late-time errors related to flow nonlinearities, we then introduce a relinearisation procedure that resets the linearisation at given time intervals. The characteristic lines defined in the augmented phase space of

https://doi.org/10.1017/jfm.2025.11092 Published online by Cambridge University Press

the Liouville equation contain all the one-point statistical information of the concentration field, and can be computed using methods for ordinary differential equations (ODEs).

This leads to a fundamentally different picture in comparison with classical approaches, in that each given Lagrangian trajectory is deterministic rather than stochastic. This new approach comes with certain analytical and computational advantages. Exploiting the fact that hyperbolic systems may be integrated backward in time without difficulty (Haller 2015), we introduce the treatment of arbitrary grids. For any chosen location of interest, the concentration field can be recovered via a marginalisation along the dimension of the random coefficients by a simple quadrature. This allows us to trace arbitrarily defined initial concentration profiles, at any Péclet number and at arbitrary locations. For simplicity, we focus here on a bidimensional derivation valid for incompressible steady flows and consider the diffusion tensor to be constant and isotropic.

In the following, the hyperbolic formulation of mixing is introduced in § 2, where the common Eulerian and Lagrangian descriptions are summarised in § 2.1 and the Liouville master equation is presented in § 2.2. The conditions to find the proper noise term are laid out in § 3, where a local analysis of two statistical moments and a description along streamline coordinates are treated in §§ 3.1 and 3.2, respectively. Then, the final description of solute plumes is laid out in § 4. A set of test cases are analysed in § 5. In order to illustrate the conceptual approach and the associated salient analytical and numerical features, we show that we recover known analytical results for the case of shear flow (Dentz *et al.* 2018) and a model for a vortex flow (Meunier & Villermaux 2003). In the latter case, we also extend existing results by considering radial diffusion and flow nonlinearities. Then, we validate the formulation and further illustrate some of its advantages by comparing with classical particle tracking computations in a heterogeneous flow field at the Darcy scale. Finally, conclusions are presented in § 6.

2. A deterministic description of mixing in Lagrangian form

2.1. *Eulerian and Lagrangian perspectives*

Transport of a passive scalar in an underlying flow field $\boldsymbol{u}(\boldsymbol{x}, t)$, here assumed to be known deterministically, is described from an Eulerian perspective by the ADE,

$$\frac{\partial c}{\partial t} + \boldsymbol{\nabla} \cdot (\boldsymbol{u} c) = \boldsymbol{\nabla} \cdot (\boldsymbol{D} \boldsymbol{\nabla} c)\,, \tag{2.1a}$$

$$c(\boldsymbol{x}, 0) = c_0(\boldsymbol{x}), \tag{2.1b}$$

where $c(\boldsymbol{x}, t)$ is the concentration at position $\boldsymbol{x}$ (in d spatial dimensions) and $\boldsymbol{D}(\boldsymbol{x}, t)$ is the scalar diffusion tensor. For a given initial condition $c_0(\boldsymbol{x})$, the ADE can be related to the FPE for the PDF $f_{\boldsymbol{X}}(\boldsymbol{x}; t) = c(\boldsymbol{x}, t) / \int_{\mathbb{R}^d} \mathrm{d}\boldsymbol{x}\, c(\boldsymbol{x}, t)$ of the locations of the solute particles composing the plume (Risken 1996; Noetinger *et al.* 2016):

$$\frac{\partial f_{\boldsymbol{X}}}{\partial t} + \boldsymbol{\nabla} \cdot (\boldsymbol{\mu} f_{\boldsymbol{X}}) = \boldsymbol{\nabla}\boldsymbol{\nabla}^{\top} : \boldsymbol{D} f_{\boldsymbol{X}}, \tag{2.2a}$$

$$f_{\boldsymbol{X}}(\boldsymbol{x}; 0) = f_{\boldsymbol{X}}^0(\boldsymbol{x}). \tag{2.2b}$$

Here the drift is $\boldsymbol{\mu}(\boldsymbol{x}, t) = \boldsymbol{u}(\boldsymbol{x}, t) + \boldsymbol{\nabla} \cdot \boldsymbol{D}(\boldsymbol{x}, t)$ and : denotes the inner tensor product.

From a Lagrangian perspective, the equivalence of the FPE and Langevin dynamics (Risken 1996) is used to describe the evolution of particles of solute (Pope 1985). In this sense, an equivalent formulation to (2.2) in Lagrangian form is given by the stochastic

https://doi.org/10.1017/jfm.2025.11092 Published online by Cambridge University Press

Langevin (or Itō) equation for particle trajectories $\boldsymbol{X}(t)$, i.e.

$$\mathrm{d}\boldsymbol{X}(t) = \boldsymbol{\mu}(\boldsymbol{X}(t), t)\mathrm{d}t + \boldsymbol{\Sigma}(\boldsymbol{X}(t), t)\mathrm{d}\boldsymbol{W}_t, \tag{2.3a}$$

$$\boldsymbol{X}(0) = \boldsymbol{X}_0, \tag{2.3b}$$

with standard Wiener increments $\mathrm{d}\boldsymbol{W}_t$, $2\boldsymbol{D} = \boldsymbol{\Sigma}\boldsymbol{\Sigma}^\top$, and the PDF of $\boldsymbol{X}_0$ given by the Eulerian initial condition $f_{\boldsymbol{X}}^0(\boldsymbol{x})$. The PDF of particle positions, which corresponds to the concentration field normalised by the total (conserved) mass, is obtained through a sampling process that can be formally expressed in the continuum limit as

$$f_{\boldsymbol{X}}(\boldsymbol{x}; t) = \overline{\delta[\boldsymbol{x} - \boldsymbol{X}(t)]}. \tag{2.4}$$

Here, $\overline{(\cdot)}$ indicates the average over all trajectories computed through (2.3), i.e. averaging over the (diffusive) noise and over the variability in the initial condition, for each position $\boldsymbol{x}$ at a given time t.

2.2. *Augmented phase space*

The framework proposed here is built upon the construction of a trajectory-based formulation for which the PDF $f_{\boldsymbol{X}}$ of the trajectories $\boldsymbol{X}(t)$ solves the FPE (2.2), but where any stochasticity is time independent. To this end, we write

$$\frac{\mathrm{d}\boldsymbol{X}(t)}{\mathrm{d}t} = \boldsymbol{u}(\boldsymbol{X}(t), t) + \boldsymbol{s}(\boldsymbol{X}(t), \boldsymbol{\Xi}, t), \tag{2.5a}$$

$$\boldsymbol{X}(0) = \boldsymbol{X}_0, \tag{2.5b}$$

with $\boldsymbol{\Xi}$ a vector of d random coefficients with PDF $f_{\boldsymbol{\Xi}}(\boldsymbol{\xi}) : \mathbb{R}^d \to \mathbb{R}^+$ and $\boldsymbol{s}(\boldsymbol{x}, \boldsymbol{\xi}, t) : \mathbb{R}^d \times \mathbb{R}^d \times \mathbb{R}^+ \to \mathbb{R}^d$ a deterministic function of the random positions, random coefficients and time. Here, d is the spatial dimensionality. The sole sources of uncertainty in (2.5*a*) are the initial condition $\boldsymbol{X}_0$ and the random coefficients $\boldsymbol{\Xi}$, and (2.5) is therefore a random differential equation (Soong 1973), as opposed to a stochastic differential equation like (2.3): while (2.5) is amenable to conventional calculus, (2.3) requires stochastic calculus. The trajectories of the present framework do not represent physical trajectories and only equality of the one-point PDF (as opposed to multi-point statistics, such as temporal correlations along trajectories) will be enforced, i.e. $f_{\boldsymbol{X}} = f_{\boldsymbol{X}}$ should solve the FPE (2.2). We show in § 3 how to chose the source term $\boldsymbol{s}$ and the PDF $f_{\boldsymbol{\Xi}}$ of the random coefficients so as to achieve this.

First, it is convenient to study (2.5) for arbitrary $\boldsymbol{s}$ and $\boldsymbol{\Xi}$. The time evolution of the joint PDF of the particle locations and random coefficients $f_{\boldsymbol{X}\boldsymbol{\Xi}}(\boldsymbol{x}, \boldsymbol{\xi}; t) : \mathbb{R}^d \times \mathbb{R}^d \times \mathbb{R}^+ \to \mathbb{R}^+$ is governed by a deterministic hyperbolic Liouville equation, which in conservative form reads as

$$\frac{\partial f_{\boldsymbol{X}\boldsymbol{\Xi}}}{\partial t} + \boldsymbol{\nabla} \cdot ([\boldsymbol{u}(\boldsymbol{x}, t) + \boldsymbol{s}(\boldsymbol{x}, \boldsymbol{\xi}, t)] f_{\boldsymbol{X}\boldsymbol{\Xi}}) = 0, \tag{2.6a}$$

$$f_{\boldsymbol{X}\boldsymbol{\Xi}}(\boldsymbol{x}, \boldsymbol{\xi}; 0) = f_{\boldsymbol{X}\boldsymbol{\Xi}}^0(\boldsymbol{x}, \boldsymbol{\xi}) = f_{\boldsymbol{X}}^0(\boldsymbol{x}) f_{\boldsymbol{\Xi}}(\boldsymbol{\xi}), \tag{2.6b}$$

where the coefficients play the role of parameters and at the initial time, the coefficients are independent and uncorrelated with the initial locations. The derivation of (2.6*a*) from (2.5*a*) is a direct application of the Liouville theorem (Moyal 1949). Alternatively, in Appendix A we provide a derivation using a distributional approach (Venturi & Karniadakis 2012; Venturi *et al.* 2013; Tartakovsky & Gremaud 2015). After marginalising

https://doi.org/10.1017/jfm.2025.11092 Published online by Cambridge University Press

over the coefficients, the normalised concentration field is recovered:

$$f_X(\boldsymbol{x};t) = \int_{\mathbb{R}^d} \mathrm{d}\boldsymbol{\xi}\; f_{X\boldsymbol{\Xi}}(\boldsymbol{x},\boldsymbol{\xi};t). \tag{2.7}$$

A strong advantage of this formulation relates to the hyperbolicity of the Liouville equation, which permits the use of the method of characteristics (Domínguez-Vázquez *et al.* 2024*a*). Points $(\boldsymbol{x},\boldsymbol{\xi})$ can be thought of elements of the augmented phase space spanned by the particle locations and random coefficient values. Let $\hat{\boldsymbol{x}}(t;\boldsymbol{\xi},\boldsymbol{x}_0,t_0)$ be a trajectory along a characteristic in this augmented phase space, parameterised by the values $\boldsymbol{\xi}$ of the random coefficients and the initial position $\boldsymbol{x}_0$ at time t_0. We allow here for arbitrary t_0 because it is useful in discussing backward trajectories below. We omit t_0 when $t_0 = 0$ and we sometimes further omit $\boldsymbol{\xi}$ and $\boldsymbol{x}_0$ for brevity. We also introduce $\hat{f}_{X\boldsymbol{\Xi}}(t;\boldsymbol{\xi},\boldsymbol{x}_0,t_0) = f_{X\boldsymbol{\Xi}}(\hat{\boldsymbol{x}}(t;\boldsymbol{\xi},\boldsymbol{x}_0,t_0),\boldsymbol{\xi};t)$, the joint PDF along the characteristics. Characteristic lines $\hat{\boldsymbol{x}}$ describe the path of what we call support particles, analogously to the more standard use of the term 'particles' in relation to advective–diffusive (Langevin) trajectories. These support particles correspond to tracking discrete points of the support of the joint PDF in the augmented phase space, carrying their joint PDF value $\hat{f}_{X\boldsymbol{\Xi}}$ along their corresponding characteristic lines. We find the following system of characteristic lines to solve (2.6) in this picture:

$$\frac{\mathrm{d}\hat{\boldsymbol{x}}(t)}{\mathrm{d}t} = \boldsymbol{u}\big(\hat{\boldsymbol{x}}(t),t\big) + \boldsymbol{s}\big(\hat{\boldsymbol{x}}(t),\boldsymbol{\xi},t\big), \tag{2.8a}$$

$$\frac{\mathrm{d}\hat{f}_{X\boldsymbol{\Xi}}(t)}{\mathrm{d}t} = -\hat{f}_{X\boldsymbol{\Xi}}(t)\boldsymbol{\nabla}\cdot\big[\boldsymbol{u}\big(\hat{\boldsymbol{x}}(t),t\big) + \boldsymbol{s}\big(\hat{\boldsymbol{x}}(t),\boldsymbol{\xi},t\big)\big], \tag{2.8b}$$

$$\hat{\boldsymbol{x}}(t_0) = \boldsymbol{x}_0, \qquad \hat{f}_{X\boldsymbol{\Xi}}(t_0) = \hat{f}^0_{X\boldsymbol{\Xi}} = f^0_X(\boldsymbol{x}_0) f_{\boldsymbol{\Xi}}(\boldsymbol{\xi}). \tag{2.8c}$$

This system of equations combines properties of the Fokker–Planck and Langevin equations, in the sense that we solve directly for the (joint) PDF, but in Lagrangian form along characteristics. Equations (2.6) or (2.8) define a crypto-deterministic (Whittaker 1943) description of the problem of passive scalar transport, i.e. all the uncertainty is contained in the initial conditions in the augmented phase space.

To recover normalised concentrations, marginalisation of the joint PDF is needed with (2.7). Due to the relationship (2.8*a*) between coefficients $\boldsymbol{\xi}$ and positions $\hat{\boldsymbol{x}}$ along characteristics, this marginalisation may also be performed directly in Lagrangian form. Indeed, we can write the following Lagrangian relation (Cramér 1946):

$$\hat{f}_{X\boldsymbol{\Xi}}(t;\boldsymbol{\xi},\boldsymbol{x}_0) = J(t;\boldsymbol{\xi},\boldsymbol{x}_0)^{-1} f^0_X(\boldsymbol{x}_0) f_{\boldsymbol{\Xi}}(\boldsymbol{\xi}), \qquad J(t;\boldsymbol{\xi},\boldsymbol{x}_0) = \left|\frac{\partial(\hat{\boldsymbol{x}},\boldsymbol{\xi})}{\partial(\boldsymbol{x}_0,\boldsymbol{\xi})}\right| = |\boldsymbol{\nabla}_{\boldsymbol{x}_0}\hat{\boldsymbol{x}}|. \tag{2.9}$$

Here $J(t)$ is the determinant of the transformation Jacobian from the initial to final time. Note that, according to (2.8*b*), $J(t)$ is unity if and only if $\boldsymbol{\nabla}\cdot(\boldsymbol{u}+\boldsymbol{s}) = 0$. Relation (2.9) offers an alternative to solving (2.8*b*) based on a transformation of random variables between the initial and later time. Using this, the marginalisation (2.7) becomes

$$f_X(\boldsymbol{x};t) = \int_{\mathbb{R}^d} \mathrm{d}\boldsymbol{\xi}\; J\big[t;\boldsymbol{\xi},\hat{\boldsymbol{x}}_0(\boldsymbol{\xi},\boldsymbol{x},t)\big]^{-1} f^0_X\big[\hat{\boldsymbol{x}}_0(\boldsymbol{\xi},\boldsymbol{x},t)\big] f_{\boldsymbol{\Xi}}(\boldsymbol{\xi}), \tag{2.10}$$

where we have introduced the backward map $\hat{\boldsymbol{x}}_0(\boldsymbol{\xi},\boldsymbol{x},t)$ for $t_0 = 0$. For arbitrary t_0, the backward map $\hat{\boldsymbol{x}}_0(t_0;\boldsymbol{\xi},\boldsymbol{x},t)$ is the solution of the characteristics (2.8*a*) given a specified

https://doi.org/10.1017/jfm.2025.11092 Published online by Cambridge University Press

final condition, i.e. for an initial time argument of $\hat{\boldsymbol{x}}$ (here t) larger than the target time along the characteristic (here t_0). Thus, we have the general equivalence $\hat{\boldsymbol{x}}_0(t_0;\boldsymbol{\xi},\boldsymbol{x},t)\equiv\hat{\boldsymbol{x}}(t_0;\boldsymbol{\xi},\boldsymbol{x},t)$, but we introduce the backward notation for intuitive clarity and to allow us to omit $t_0=0$ for notational simplicity. In practice, the backward map can be computed in one of two ways: (i) by integrating (2.8*a*) backward as just described; or (ii) given the forward solution, by inverting $\hat{\boldsymbol{x}}[t;\boldsymbol{\xi},\hat{\boldsymbol{x}}_0(t_0;\boldsymbol{\xi},\boldsymbol{x},t),t_0]=\boldsymbol{x}$.

Since the sole sources of stochasticity in the description are the initial condition and the random coefficients, moments may be directly obtained from the characteristics by averaging over their PDFs (see Appendix B). Moreover, due to linearity, quantities associated with any initial condition can be constructed by summing over the solutions for deterministic (i.e. Dirac-delta) initial conditions, after integrating over the random coefficients for each initial point. We make explicit use of this fact in § 4.

3. Equivalence conditions

3.1. *Closed two-moment description*

We are now ready to determine the source term $\boldsymbol{s}$ such that the Liouville equation (2.5) marginalised along the coefficients leads to the FPE (2.2). To this end, we derive conditions for $\boldsymbol{s}$ by comparing moments of the FPE with those of the system (2.5). Taking moments of the FPE will in general lead to a closure problem. Instead, we locally linearise the flow in order to obtain a closed system. Details on the derivation of a closed two-moment description of $\boldsymbol{X}(t)$ based on (2.5) are given in Appendix B. We focus here on the case of a spatially independent dispersion tensor, and we seek a simple form of $\boldsymbol{s}$ capable of matching the first two moments of the FPE (2.2). In this case, it turns out to be sufficient to take a noise term that is independent of position and linear in the random coefficient values, i.e.

$$\boldsymbol{s}(\boldsymbol{\xi},t)=\boldsymbol{\varphi}(t)\boldsymbol{\xi}, \tag{3.1}$$

where, by definition, $\boldsymbol{\varphi}(t):\mathbb{R}^+\to\mathbb{R}^d\times\mathbb{R}^d$ is the matrix containing the first derivatives of $\boldsymbol{s}$ with respect to the coefficients $\boldsymbol{\xi}$. We also assume for simplicity that the underlying flow field is steady (i.e. the Eulerian field $\boldsymbol{u}$ is independent of time t), two-dimensional ($d=2$) and incompressible ($\boldsymbol{\nabla}\cdot\boldsymbol{u}=0$). Then, the results in Appendix B read

$$\frac{\mathrm{d}\overline{\boldsymbol{X}}(t)}{\mathrm{d}t}=\boldsymbol{u}\big[\overline{\boldsymbol{X}}(t)\big]+\boldsymbol{\varphi}(t)\overline{\boldsymbol{\Xi}}, \tag{3.2a}$$

$$\frac{\mathrm{d}\boldsymbol{\kappa}(t)}{\mathrm{d}t}=\boldsymbol{\epsilon}(t)\boldsymbol{\kappa}(t)\ +\boldsymbol{\kappa}(t)\boldsymbol{\epsilon}(t)^\top+\boldsymbol{\varphi}(t)\boldsymbol{\zeta}(t)+[\boldsymbol{\varphi}(t)\boldsymbol{\zeta}(t)]^\top, \tag{3.2b}$$

$$\frac{\mathrm{d}\boldsymbol{\zeta}(t)}{\mathrm{d}t}=\boldsymbol{\zeta}(t)\boldsymbol{\epsilon}(t)^\top+\boldsymbol{\theta}\boldsymbol{\varphi}(t)^\top, \tag{3.2c}$$

$$\overline{\boldsymbol{X}}(0)=\overline{\boldsymbol{X}}^0,\quad \boldsymbol{\kappa}(0)=\boldsymbol{\kappa}^0,\quad \boldsymbol{\zeta}(0)=\boldsymbol{0}. \tag{3.2d}$$

For each given initial position, this system involves the velocity gradient tensor at the average particle location,

$$\boldsymbol{\epsilon}(t)=(\boldsymbol{\nabla}\boldsymbol{u}[\overline{\boldsymbol{X}}(t)])^\top, \tag{3.3}$$

along with the first two moments of the phase space variables, i.e. the averages $\overline{\boldsymbol{X}}(t)$ and $\overline{\boldsymbol{\Xi}}$ and the correlations $\kappa_{ij}(t)=\overline{X_i'X_j'}(t)$, $\zeta_{ij}(t)=\overline{\Xi_i'X_j'}(t)$ and $\theta_{ij}=\overline{\Xi_i'\Xi_j'}$. Inspired by previous results for Brownian motion and the Ornstein-Uhlenbeck process, see

https://doi.org/10.1017/jfm.2025.11092 Published online by Cambridge University Press

Domínguez-Vázquez *et al.* (2024*b*) and Appendix C, we take the coefficients to follow independent standard normal distributions, so that $\overline{\boldsymbol{\Xi}} = \mathbf{0}$ and $\boldsymbol{\theta}$ is the identity matrix, and

$$f_{\boldsymbol{\Xi}}(\boldsymbol{\xi}) = \frac{\exp\left(-\frac{1}{2}\sum_{i=1}^{d}\xi_i^2\right)}{(2\pi)^{d/2}}. \tag{3.4}$$

This turns out to be sufficient to capture the more general, linearised process examined here.

We now equate the results for the first two moments from (3.2*a*) and (3.2*b*) to the equivalent results for the FPE or the ADE; see, for example, De Barros *et al.* (2012) or Aquino & Bolster (2017) where the moment equations of the ADE are analysed. This leads to the following two conditions:

$$\boldsymbol{\varphi}(t)\overline{\boldsymbol{\Xi}} = \mathbf{0}, \tag{3.5a}$$

$$\boldsymbol{\varphi}(t)\boldsymbol{\zeta}(t) + [\boldsymbol{\varphi}(t)\boldsymbol{\zeta}(t)]^{\top} = 2\boldsymbol{D}. \tag{3.5b}$$

The first condition states that the contribution of the noise to the average drift is zero and it is fulfilled by $\overline{\boldsymbol{\Xi}} = \mathbf{0}$. The second sets the contribution of the noise to the second moments. To do so, it is convenient to employ a streamline coordinate system, i.e. a locally orthogonal reference frame where one of the basis vectors is locally aligned with the velocity vector, as shown below. In what follows we will further simplify the description by considering spatially constant and isotropic dispersion, so that $\boldsymbol{D} = D\delta_{ij}$, where D is a dispersion (or diffusion) coefficient.

3.2. *Streamline coordinate frame*

To determine the matrix $\boldsymbol{\varphi}(t)$ from (3.5*b*) explicitly, we move to the streamline coordinate frame, where it is upper triangular. To see this, consider first the distance vector between two nearby streamlines in an orthogonal frame that follows one of them and has the x-direction oriented along it (Winter 1982). In this frame, we locally linearise the flow field following Dentz *et al.* (2016). We then restore dispersion to this picture by looking at the evolution of the position $\boldsymbol{z}(t)$ of a diffusive particle in this frame, whose evolution is governed by the following FPE (see Dentz *et al.* 2018 and Appendix D):

$$\frac{\partial f_{\boldsymbol{Z}}}{\partial t} + \boldsymbol{\nabla}\cdot\boldsymbol{\epsilon}\boldsymbol{z} f_{\boldsymbol{Z}} = D\nabla^2 f_{\boldsymbol{Z}}, \qquad f_{\boldsymbol{Z}}(\boldsymbol{z};t_0) = f_{\boldsymbol{Z}}^0(\boldsymbol{z}). \tag{3.6}$$

Here $\boldsymbol{\epsilon}(t;\boldsymbol{x}_0,t_0)$ is the velocity gradient tensor in the streamline coordinate system,

$$\boldsymbol{\epsilon}(t;\boldsymbol{x}_0,t_0) = \begin{bmatrix} \alpha(t;\boldsymbol{x}_0,t_0) & \gamma(t;\boldsymbol{x}_0,t_0) \\ 0 & -\alpha(t;\boldsymbol{x}_0,t_0) \end{bmatrix}, \tag{3.7}$$

whose components are the shear rate $\gamma(t;\boldsymbol{x}_0,t_0)$ and the elongation rate $\alpha(t;\boldsymbol{x}_0,t_0)$ along the streamline; see (D8). This description can be extended to three-dimensional flows by the use of the so-called Protean coordinate frame (Lester *et al.* 2018).

Using (3.5*b*) and (3.2*c*) and exploiting the upper-triangular form of the velocity gradient tensor in this frame, we obtain the components of $\boldsymbol{\varphi}(t;\boldsymbol{x}_0,t_0)$ as

$$\begin{aligned} \varphi_{11}(t) &= \frac{D}{\zeta_{11}(t)}\left(\frac{\zeta_{21}(t)^2}{\zeta_{22}(t)^2}+1\right), & \varphi_{12}(t) &= -\frac{D\zeta_{21}(t)}{\zeta_{22}(t)^2}, \\ \varphi_{21}(t) &= 0, & \varphi_{22}(t) &= \frac{D}{\zeta_{22}(t)}, \end{aligned} \tag{3.8}$$

https://doi.org/10.1017/jfm.2025.11092 Published online by Cambridge University Press

where the components of the correlation matrix $\boldsymbol{\zeta}(t;\boldsymbol{x}_0,t_0)$ obey the Bernoulli ((3.9*a*) and (3.9*d*)) and linear ((3.9*b*) and (3.9*c*)) differential equations

$$\frac{\mathrm{d}\zeta_{11}(t)}{\mathrm{d}t}-\alpha(t)\zeta_{11}(t)=\frac{D}{\zeta_{11}(t)}\left(\frac{\zeta_{21}(t)^2}{\zeta_{22}(t)^2}+1\right),\qquad \zeta_{11}(t_0)=0, \tag{3.9a}$$

$$\frac{\mathrm{d}\zeta_{12}(t)}{\mathrm{d}t}+\alpha(t)\zeta_{12}(t)=0,\qquad \zeta_{12}(t_0)=0, \tag{3.9b}$$

$$\frac{\mathrm{d}\zeta_{21}(t)}{\mathrm{d}t}+\left(\frac{D}{\zeta_{22}(t)^2}-\alpha(t)\right)\zeta_{21}(t)=\gamma(t)\zeta_{22}(t),\qquad \zeta_{21}(t_0)=0, \tag{3.9c}$$

$$\frac{\mathrm{d}\zeta_{22}(t)}{\mathrm{d}t}+\alpha(t)\zeta_{22}(t)=\frac{D}{\zeta_{22}(t)},\qquad \zeta_{22}(t_0)=0, \tag{3.9d}$$

with solutions

$$\begin{aligned}&\zeta_{11}(t)=\left[2Dp(t)\int_{t_0}^{t}\frac{\mathrm{d}t'}{p(t')}\left(\frac{\zeta_{21}(t')^2}{\zeta_{22}(t')^2}+1\right)\right]^{1/2},\quad \zeta_{12}(t)=0,\\ &\zeta_{21}(t)=\frac{1}{q(t)}\int_{t_0}^{t}\mathrm{d}t'q(t')\gamma(t')\zeta_{22}(t'),\qquad \zeta_{22}(t)=\left(\frac{2D}{p(t)}\int_{t_0}^{t}\mathrm{d}t'p(t')\right)^{1/2},\end{aligned} \tag{3.10}$$

where

$$p(t)=\mathrm{e}^{2\int_{t_0}^{t}\mathrm{d}t\alpha(t)},\quad q(t)=\exp\left[\int_{t_0}^{t}\mathrm{d}t\left(\frac{D}{\zeta_{22}(t)^2}-\alpha(t)\right)\right]. \tag{3.11}$$

With the source term $\boldsymbol{\varphi}(t)$ defined by (3.8), the hyperbolic description is fully characterised. Using (2.6) and (3.1), the Liouville master equation in conservative form is

$$\frac{\partial f_{\boldsymbol{Z}\boldsymbol{\Xi}}}{\partial t}+\boldsymbol{\nabla}\cdot(\boldsymbol{\epsilon}\boldsymbol{z}+\boldsymbol{\varphi}\boldsymbol{\xi})\,f_{\boldsymbol{Z}\boldsymbol{\Xi}}=0,\qquad f_{\boldsymbol{Z}\boldsymbol{\Xi}}(\boldsymbol{z},\boldsymbol{\xi};t_0)=f^0_{\boldsymbol{Z}}(\boldsymbol{z})f_{\boldsymbol{\Xi}}(\boldsymbol{\xi}), \tag{3.12}$$

and the corresponding system of random differential equations(2.5) reads

$$\frac{\mathrm{d}Z_1(t)}{\mathrm{d}t}=\alpha(t)Z_1+\gamma(t)Z_2+\Xi_1\varphi_{11}(t)+\Xi_2\varphi_{12}(t),\qquad Z_1(t_0)=Z_1^0, \tag{3.13a}$$

$$\frac{\mathrm{d}Z_2(t)}{\mathrm{d}t}=-\alpha(t)Z_2+\Xi_2\varphi_{22}(t),\qquad Z_2(t_0)=Z_2^0. \tag{3.13b}$$

For a given choice of distribution for the initial condition $\boldsymbol{Z}^0$ and random variables $\boldsymbol{\Xi}$, the system (3.13) can be solved numerically using Monte Carlo method. Since for any given value of these random variables, (3.13) becomes an ODE system, we can say more about this system analytically using the method of characteristics as before. The characteristic lines $\hat{\boldsymbol{z}}(t;\boldsymbol{\xi},\boldsymbol{x}_0,t_0)$ of (3.12) solve

$$\frac{\mathrm{d}\hat{\boldsymbol{z}}(t)}{\mathrm{d}t}=\boldsymbol{\epsilon}(t)\hat{\boldsymbol{z}}(t)+\boldsymbol{\varphi}(t)\boldsymbol{\xi},\qquad \hat{\boldsymbol{z}}(t_0)=\boldsymbol{z}_0, \tag{3.14a}$$

$$\frac{\mathrm{d}\hat{f}_{\boldsymbol{Z}\boldsymbol{\Xi}}(t)}{\mathrm{d}t}=0,\qquad \hat{f}_{\boldsymbol{Z}\boldsymbol{\Xi}}(t_0)=f^0_{\boldsymbol{Z}}(\boldsymbol{z}_0)f_{\boldsymbol{\Xi}}(\boldsymbol{\xi}). \tag{3.14b}$$

https://doi.org/10.1017/jfm.2025.11092 Published online by Cambridge University Press

With the previous results, the analytical solution for these characteristic lines can be expressed as the sum of a homogeneous and a particular solution,

$$\hat{\boldsymbol{z}}(t) = \boldsymbol{B}(t)\boldsymbol{z}_0 + \boldsymbol{\zeta}(t)^{\top}\boldsymbol{\xi}, \tag{3.15}$$

such that the homogeneous part relates to the deformations without considering diffusion, i.e. to the kinematics of the flow according to (D6). An analytical solution for this part is given in Dentz *et al.* (2016, 2018), from which

$$\begin{aligned} B_{11}(t) &= \frac{v(t)}{v(t_0)}, \quad & B_{12}(t) &= v(t_0)v(t)\int_{t_0}^{t} \mathrm{d}t' \frac{\gamma(t')}{v(t')^2}, \\ B_{21}(t) &= 0, & B_{22}(t) &= \frac{v(t_0)}{v(t)}. \end{aligned} \tag{3.16}$$

In terms of the moment description (3.2), it corresponds to the average path of the blob of solute. The particular solution, on the other hand, encodes the effect of diffusion in terms of the random coefficients. It produces deviations from the average path, such that characteristic lines with large values of the coefficients $\boldsymbol{\xi}$ deviate more from the average solution encoded in the homogeneous part.

Then, the complete solution to the characteristic system (3.14), marginalised along the coefficients to obtain the concentration field in the streamline coordinate system, is

$$f_{\boldsymbol{Z}}(\boldsymbol{z}; t) = \int_{\mathbb{R}^d} \mathrm{d}\boldsymbol{\xi}\; f_{\boldsymbol{Z}}^0\big[\hat{\boldsymbol{z}}_0(\boldsymbol{\xi}, \boldsymbol{z}, t)\big] f_{\boldsymbol{\Xi}}(\boldsymbol{\xi}), \tag{3.17}$$

where from (3.15) the backward map $\hat{\boldsymbol{z}}_0(\boldsymbol{\xi}, \boldsymbol{z}, t)$ is simply

$$\hat{\boldsymbol{z}}_0(\boldsymbol{\xi}, \boldsymbol{z}, t) = \boldsymbol{B}(t)^{-1}\big(\boldsymbol{z} - \boldsymbol{\zeta}(t)^{\top}\boldsymbol{\xi}\big). \tag{3.18}$$

In the particular case of a deterministic (point) initial condition, where $f_{\boldsymbol{Z}}^0(\boldsymbol{z}) = \delta(\boldsymbol{z})$, the properties of the Dirac delta can be used to simplify the integral in (3.17), leading to the Gaussian distribution

$$f_{\boldsymbol{Z}}(\boldsymbol{z}; t) = \frac{1}{2\pi\,\det[\boldsymbol{\zeta}(t)]} \exp\left(-\frac{1}{2}\boldsymbol{z}^{\top}\big[\boldsymbol{\zeta}(t)^{\top}\boldsymbol{\zeta}(t)\big]^{-1}\boldsymbol{z}\right), \tag{3.19}$$

with centred second moments $\boldsymbol{\kappa}(t) = \boldsymbol{\zeta}(t)^{\top}\boldsymbol{\zeta}(t)$ and $\boldsymbol{\kappa}(0) = \boldsymbol{\kappa}^0 = \boldsymbol{0}$. Note that the choice of independent, normally distributed random coefficients ensures this result is exact for a linear flow with a constant velocity gradient tensor (Van Kampen 1992; Risken 1996; Bolster, Dentz & Le Borgne 2011; Dentz *et al.* 2018). More generally, for other forms of $f_{\boldsymbol{Z}}^0$ of interest, (3.17) can be easily computed numerically.

4. Evolution of solute plumes in arbitrary grids

In this section we collect our results in order to describe the evolution of an arbitrary concentration field at arbitrary spatial locations and times. The description in the augmented phase space requires a marginalisation along the random coefficients $\boldsymbol{\Xi}$ to recover the PDF of solute particles $f_{\boldsymbol{X}}$. As already mentioned, this marginalisation can be performed independently for any given initial condition; see the end of § 2. Thus, the local analysis leads directly to a solution for the full solute plume by repeating it for each point of space where the initial concentration profile is non-zero. In other words, an initial solute concentration profile with arbitrary shape can be evolved in time with the system (2.8), taking the source term $\boldsymbol{s}$ from (3.1) and (3.8). As a result, the hyperbolic description introduced here can be used to construct numerical algorithms similar to those based on

https://doi.org/10.1017/jfm.2025.11092 Published online by Cambridge University Press

the concept of lamellae previously introduced in the literature (Meunier & Villermaux 2010; Martínez-Ruiz *et al.* 2018; Sen *et al.* 2020; Meunier & Villermaux 2022; Pushenko *et al.* 2025).

Reintroducing the streamline associated with a given initial point $\boldsymbol{x}_0$ at $t_0 = 0$ and rotating back to the Eulerian frame from the streamline frame, see the discussion at the beginning of § 3.2 and (3.15), the support particles describe trajectories given by

$$\hat{\boldsymbol{x}}(t;\boldsymbol{\xi},\boldsymbol{x}_0) = \boldsymbol{x}(t;\boldsymbol{x}_0) + \boldsymbol{A}(t;\boldsymbol{x}_0)\boldsymbol{\zeta}(t;\boldsymbol{x}_0)^{\top}\boldsymbol{\xi}, \tag{4.1}$$

where $\boldsymbol{x}(t;\boldsymbol{x}_0)$ are fluid trajectories (D1), i.e. the flow map (Haller & Yuan 2000; Shadden, Lekien & Marsden 2005; Haller 2015). For a detailed derivation of (4.1), see Appendix E. The last term in (4.1) adds the contribution of diffusion encoded in the random coefficients, where $\boldsymbol{A}(t;\boldsymbol{x}_0)$ is the rotation matrix to the streamline frame computed from (D5) for each initial location $\boldsymbol{x}_0$ starting at $t_0 = 0$. Similarly, $\boldsymbol{\zeta}(t;\boldsymbol{x}_0)$ is computed from (3.10), which involves the tracing of the upper-triangular strain-rate tensor $\boldsymbol{\epsilon}(t;\boldsymbol{x}_0)$ in time using (3.7). The corresponding joint PDF is

$$\hat{f}_{X\Xi}(t;\boldsymbol{\xi},\boldsymbol{x}_0) = f_X^0\big[\hat{\boldsymbol{x}}(t;\boldsymbol{\xi},\boldsymbol{x}_0)\big] f_{\Xi}(\boldsymbol{\xi}), \tag{4.2}$$

where we note that $J(t) = 1$ for an incompressible flow field and $\boldsymbol{x}$-independent source term $\boldsymbol{s} = \boldsymbol{\varphi}\boldsymbol{\xi}$.

The backward map $\hat{\boldsymbol{x}}_0$ for the support particle at position $\hat{\boldsymbol{x}}(t;\tilde{\boldsymbol{\xi}},\boldsymbol{x}_0)$ is given by (Appendix E)

$$\hat{\boldsymbol{x}}_0\big[\boldsymbol{\xi},\hat{\boldsymbol{x}}(t;\tilde{\boldsymbol{\xi}},\boldsymbol{x}_0),t\big] = \boldsymbol{x}_0 + \boldsymbol{A}(0;\boldsymbol{x}_0)\boldsymbol{B}(t;\boldsymbol{x}_0)^{-1}\boldsymbol{\zeta}(t;\boldsymbol{x}_0)^{\top}(\tilde{\boldsymbol{\xi}} - \boldsymbol{\xi}), \tag{4.3}$$

where $\tilde{\boldsymbol{\xi}}$ denotes the coefficients used in the tracing of support particles forward in time (see below) and $\boldsymbol{B}(t;\boldsymbol{x}_0)$ is the homogeneous solution (3.16) at time t corresponding to each initial location $\boldsymbol{x}_0$ at time $t_0 = 0$. Using (2.10), the evolution of an arbitrary initial normalised concentration profile at the support particle locations given in (4.1) is described by the quadrature

$$f_X\big[\hat{\boldsymbol{x}}(t;\tilde{\boldsymbol{\xi}},\boldsymbol{x}_0);t\big] = \int_{\mathbb{R}^d} \mathrm{d}\boldsymbol{\xi}\; f_X^0\big(\hat{\boldsymbol{x}}_0\big[\boldsymbol{\xi},\hat{\boldsymbol{x}}\big(t;\tilde{\boldsymbol{\xi}},\boldsymbol{x}_0\big),t\big]\big) f_{\Xi}(\boldsymbol{\xi}). \tag{4.4}$$

Intuitively, the rationale for using different forward and backward coefficients is as follows. Suppose one takes a set of initial points $\boldsymbol{x}_0$ that lie within the non-zero region of the initial concentration field and traces their characteristics in the augmented phase space for some set of random coefficients $\tilde{\boldsymbol{\xi}}$. At a given time t, these points will be arranged on some deformed grid $\hat{\boldsymbol{x}}(t;\tilde{\boldsymbol{\xi}},\boldsymbol{x}_0)$ in real space. We wish to compute the normalised concentration f_X on this grid. While an arbitrary initial choice of values of $\boldsymbol{x}_0$ and $\tilde{\boldsymbol{\xi}}$ will generally be mapped to a set of distinct points, in general there exists a combination of different values of initial positions and random coefficients that contributes to the concentration on the same final point on the deformed grid. Tracing backward using a different set of random coefficients $\boldsymbol{\xi}$ provides a convenient way of finding the points $\hat{\boldsymbol{x}}_0[\boldsymbol{\xi},\hat{\boldsymbol{x}}(t;\tilde{\boldsymbol{\xi}},\boldsymbol{x}_0),t]$ on the initial concentration profile whose contributions should be integrated over in (4.4).

The result in (4.4) provides the concentration field at any time t in an unstructured Lagrangian grid given by (4.1), starting from an arbitrary initial grid with a discretisation of $\boldsymbol{x}_0$ and $\boldsymbol{\xi}$ at time $t_0 = 0$. Figure 1(*a*) illustrates this for a deterministic (point) initial condition and figure 1(*b*) for a stochastic (Gaussian) initial condition (see also Appendix C). As with Lagrangian methods, this formulation offers the benefit of only tracking the parcel of space where the solute is present. Interpolation to Eulerian grids for post-processing or coupling with other Eulerian solvers in classical Lagrangian

https://doi.org/10.1017/jfm.2025.11092 Published online by Cambridge University Press

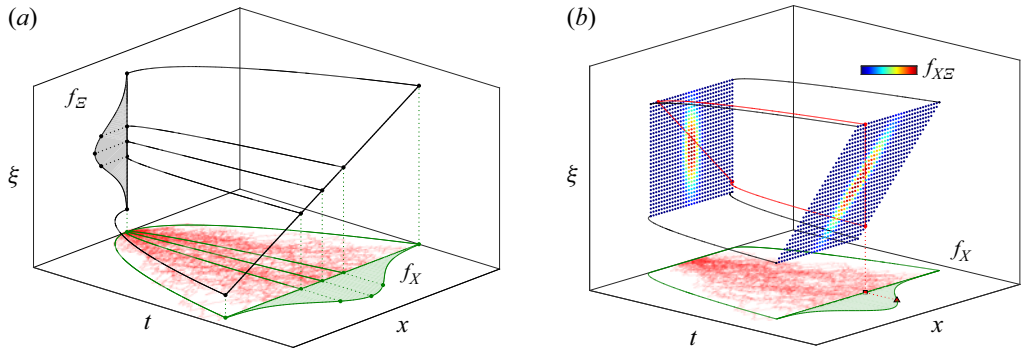


Figure 1. Evolution of the PDF of particle positions for a deterministic (point) initial condition in (*a*) and stochastic (Gaussian) initial condition in (*b*). The red line in (*b*) at the initial time corresponds to the backward map $\hat{x}_0$, given by (4.6), of the arbitrarily chosen point x, which is depicted as the red square in the support of f_X at time t, and the value of the PDF at that point, $f_X(\mathrm{x};\, t)$, depicted as a red triangle, is given by relation (4.7).

approaches, however, may be complicated (Domínguez-Vázquez *et al.* 2024*a*), sometimes restricting the use of Lagrangian methods for hyperbolic systems (Guerrero-Hurtado *et al.* 2023). Using the present method, we can go further and adapt (4.4) to allow us to impose an arbitrary choice of grid at each time t, such that complex domains can be easily studied, and post-processing facilitated by eliminating any interpolation step.

We require the concentration field at time t at some specified location $\boldsymbol{x}$. The key ingredients here are that the trajectories of support particles in the augmented phase space are fully determined by the value of the initial position and of the random coefficients and can be traced both forward and backward in time according to the explicit solution (3.15), and that if the random coefficients are zero the streamline associated with the initial position is recovered. The initial point along the local streamline corresponding to $\boldsymbol{x}$ can thus be traced back using the backward flow map,

$$\hat{\boldsymbol{x}}_0(\boldsymbol{x}, t) = \boldsymbol{x}(0; \boldsymbol{x}, t), \tag{4.5}$$

where $\boldsymbol{x}$ solves the streamline equation (D1), and the full backward map is (Appendix E)

$$\hat{\boldsymbol{x}}_0(\boldsymbol{\xi}, \boldsymbol{x}, t) = \hat{\boldsymbol{x}}_0(\boldsymbol{x}, t) - \boldsymbol{A}\big[0; \hat{\boldsymbol{x}}_0(\boldsymbol{x}, t)\big]\boldsymbol{B}\big[t; \hat{\boldsymbol{x}}_0(\boldsymbol{x}, t)\big]^{-1}\boldsymbol{\zeta}\big[t; \hat{\boldsymbol{x}}_0(\boldsymbol{x}, t)\big]^{\top}\boldsymbol{\xi}. \tag{4.6}$$

Using (2.10), this leads to the desired relation to compute the normalised concentration of the plume at an arbitrary location:

$$f_X(\boldsymbol{x}; t) = \int_{\mathbb{R}^d} \mathrm{d}\boldsymbol{\xi}\; f_X^0\big[\hat{\boldsymbol{x}}_0(\boldsymbol{\xi}, \boldsymbol{x}, t)\big] f_{\boldsymbol{\Xi}}(\boldsymbol{\xi}). \tag{4.7}$$

Relation (4.4), and equivalently (4.7), remain valid while the local linearisation of the flow field used in § 3.2 holds. An estimate of this time frame is given by the diffusion time $\tau_D = l_c^2/D$, with l_c the characteristic length of the flow, such that for $t \lesssim \tau_D$, the support particles stay sufficiently close to their corresponding streamline. For longer times, or simply to increase accuracy, we can make use of a relinearisation procedure by successively applying relation (4.7) at discrete time intervals to recompute the linearisation. Consider a given set of $N_t + 1$ discrete times, e.g. uniformly distributed $t_j = t_0 + j\Delta t$, with $j = 0, \ldots, N_t$. The solution at time t_{j+1} is then obtained from the solution in the previous time by

https://doi.org/10.1017/jfm.2025.11092 Published online by Cambridge University Press

$$f_X(\boldsymbol{x}; t_{j+1}) = \int_{\mathbb{R}^d} \mathrm{d}\boldsymbol{\xi}\ f_X\big[\hat{\boldsymbol{x}}_0(t_j; \boldsymbol{\xi}, \boldsymbol{x}, t_{j+1}), t_j\big] f_{\boldsymbol{\Xi}}(\boldsymbol{\xi}). \tag{4.8}$$

A spatial interpolant of the concentration field f_X at each time t_j, $j > 0$, is required to evaluate the integrand in (4.8). Our hyperbolic formulation allows one to target arbitrary locations at which the concentration field is computed from (4.7), which means the interpolation nodes can be chosen arbitrarily. At each relinearisation time, the integral in the random coefficients $\boldsymbol{\xi}$ is also rediscretised according to any procedure of choice. In the examples that follow, we employ a uniform grid discretisation together with a trapezoidal rule along each dimension at the initial time, and if relinearisation is employed, the same procedure is used at each time t_j.

5. Example applications

In the following, we apply the proposed hyperbolic formulation to four different test flows: two flows characterised by a constant velocity gradient tensor, an idealised vortex flow and a heterogeneous Darcy flow.

5.1. *Constant strain-rate tensor*

We first consider two canonical cases in which the velocity gradient tensor $\boldsymbol{\epsilon}$ is constant in space.

5.1.1. *Simple shear flow*

In the case of a pure linear shear flow, the velocity field is given by

$$\boldsymbol{u}(\boldsymbol{x}) = \gamma x_2 \boldsymbol{e}_1. \tag{5.1}$$

For this case, (3.8) and (3.10) give

$$\begin{aligned} \varphi_{11}(t) &= \frac{D\left(1 + \frac{1}{4}\gamma^2 t^2\right)}{\sqrt{2Dt + \frac{1}{6}D\gamma^2 t^3}}, & \varphi_{12}(t) &= -\frac{\gamma\sqrt{Dt}}{2\sqrt{2}}, \\ \varphi_{21}(t) &= 0, & \varphi_{22}(t) &= \sqrt{\frac{D}{2t}}, \end{aligned} \tag{5.2}$$

and

$$\begin{aligned} \zeta_{11}(t) &= \sqrt{2Dt + \frac{1}{6}D\gamma^2 t^3}, & \zeta_{12}(t) &= 0, \\ \zeta_{21}(t) &= \frac{1}{2}\gamma t\sqrt{2Dt}, & \zeta_{22}(t) &= \sqrt{2Dt}. \end{aligned} \tag{5.3}$$

These results can be used to obtain the characteristics from (3.15):

$$\hat{\boldsymbol{z}}(t; \boldsymbol{\xi}, \boldsymbol{z}_0) = \begin{bmatrix} z_{0,1} + \gamma t z_{0,2} + \xi_1\sqrt{2Dt + \frac{1}{6}D\gamma^2 t^3} + \frac{1}{2}\xi_2\gamma t\sqrt{2Dt} \\ z_{0,2} + \xi_2\sqrt{2Dt} \end{bmatrix}. \tag{5.4}$$

Using the moment description (3.2), the evolution of the covariance matrix $\boldsymbol{\kappa}(t)$ can also be obtained analytically, i.e.

https://doi.org/10.1017/jfm.2025.11092 Published online by Cambridge University Press

$$\kappa_{11}(t) = \kappa_{11}^0 + 2\gamma t\kappa_{12}^0 + \gamma^2 t^2 \kappa_{22}^0 + 2Dt + \frac{2}{3}D\gamma^2 t^3, \tag{5.5a}$$

$$\kappa_{12}(t) = \kappa_{12}^0 + \gamma t\kappa_{22}^0 + D\gamma t^2, \tag{5.5b}$$

$$\kappa_{22}(t) = \kappa_{22}^0 + 2Dt, \tag{5.5c}$$

in agreement with the results in Bolster *et al.* (2011) and Dentz *et al.* (2018). We note that the asymptotic decay of the maximum concentration $c_m(t) \propto 1/\sqrt{\det[\boldsymbol{\kappa}(t)]}$ at long times in a simple shear flow is $c_m(t) \propto t^{-2}$, which is not captured by the lamellae model because diffusion along the lamella orientation is neglected (Souzy *et al.* 2018).

Relations (5.2) and (5.3) can be used to describe the evolution of any initial concentration profile. For example, the case of a point source is given analytically by (3.19), which leads to the classical result (Risken 1996)

$$f_{\boldsymbol{Z}}(\boldsymbol{z};\, t) = \frac{\exp\left(-\dfrac{1}{2}\boldsymbol{z}^\top \boldsymbol{\kappa}^{-1}(t)\boldsymbol{z}\right)}{2\pi\sqrt{\det[\boldsymbol{\kappa}(t)]}}, \tag{5.6}$$

with

$$\kappa_{11}(t) = 2Dt + \frac{2}{3}D\gamma^2 t^3, \qquad \kappa_{12}(t) = D\gamma t^2, \qquad \kappa_{22}(t) = 2Dt. \tag{5.7}$$

If we consider an initial condition composed by N_I discrete point injection locations $\tilde{\boldsymbol{x}}_k$ along the horizontal axis,

$$f_{\boldsymbol{X}}^0(\boldsymbol{x}) = \frac{1}{N_I}\sum_{k=1}^{N_I} \delta(\boldsymbol{x} - \tilde{\boldsymbol{x}}_k), \tag{5.8}$$

the PDF of solute particle locations is given analytically by

$$f_{\boldsymbol{X}}(\boldsymbol{x};\, t) = \frac{1}{N_I}\sum_{k=1}^{N_I} \frac{\exp\left[-\dfrac{1}{2}(\boldsymbol{x} - \tilde{\boldsymbol{x}}_k)^\top \boldsymbol{\kappa}(t)^{-1}(\boldsymbol{x} - \tilde{\boldsymbol{x}}_k)\right]}{2\pi\sqrt{\det[\boldsymbol{\kappa}(t)]}}. \tag{5.9}$$

An example with $P = 2$ is shown in figure 2(*a–d*), evaluated at discrete support particle locations $\hat{\boldsymbol{x}}_k = \tilde{\boldsymbol{x}}_k + \hat{\boldsymbol{z}}$, using (5.4) for $\hat{\boldsymbol{z}}$ with $\boldsymbol{z}_0 = \boldsymbol{0}$, see also (4.1), where by virtue of (5.1) one has $\boldsymbol{A}(t) = \boldsymbol{\mathcal{I}}$, the identity matrix. The blob evolution of arbitrary initial conditions can also be computed with (4.4). In figure 2(*e–h*) we show the evolution of a multimodal distribution based on skew-normal and Gaussian distributions used as an initial condition, by integrating (4.4) numerically with the trapezoidal rule.

5.1.2. *Straining flow with shear*

Consider now a velocity field given by

$$\boldsymbol{u}(\boldsymbol{x}) = (\alpha x_1 + \gamma x_2)\boldsymbol{e}_1 - \alpha x_2 \boldsymbol{e}_2. \tag{5.10}$$

This corresponds to the most general form of gradient tensor (3.7) needed to treat the incompressible, time-dependent case in the streamline frame. This example is of special importance because at the initial time $\boldsymbol{\zeta}(0) = \boldsymbol{0}$ in general, and the source term $\boldsymbol{\varphi}(t)$ given by (3.8) becomes unbounded, causing numerical issues in the computation of characteristic lines. This occurs because the characteristics deviate from the local streamline infinitely fast at arbitrarily small times, and it is consistent with the small-time limit of the FPE, which leads to infinitely fast initial velocities (Zaslavsky 2002).

https://doi.org/10.1017/jfm.2025.11092 Published online by Cambridge University Press

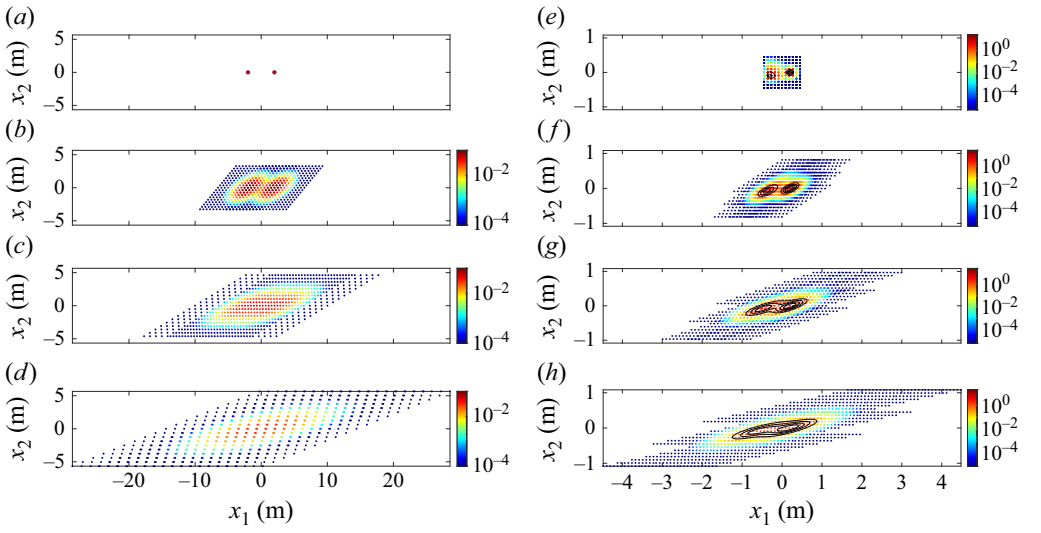


Figure 2. Evolution of the PDF of solute particle locations $f_{\boldsymbol{X}}$ in a shear flow from a deterministic initial condition composed of two injection points according to (5.8) with $(\tilde{x}_{1,1}, \tilde{x}_{2,1}) = (-2, 0)$ and $(\tilde{x}_{1,2}, \tilde{x}_{2,2}) = (2, 0)$, with $D = 0.2\ \mathrm{m^2 s^{-1}}$ at (*a*) $t = 0$ s, (*b*) $t = 1.67$ s, (*c*) $t = 3.33$ s and (*d*) $t = 5$ s; and a multimodal initial condition with $D = 2 \times 10^{-3}\ \mathrm{m^2 s^{-1}}$ at (*e*) $t = 0$ s, (*f*) $t = 1.33$ s, (*g*) $t = 2.67$ s and (*h*) $t = 4$ s. For both cases, $\gamma = 1\ \mathrm{s^{-1}}$.

This singularity can be avoided by assuming a constant strain-rate tensor during a small initial time step, over which the characteristics can be obtained analytically with the following results, before continuing the computation numerically.

In this case, (3.8) and (3.10) give

$$\varphi_{11}(t) = \frac{\sqrt{D}\left(\mathrm{e}^{\alpha t}\left(4\alpha^2+\gamma^2\right)\sinh^2[\alpha t] + \alpha\gamma^2\mathrm{e}^{\alpha t}\left(1-\mathrm{e}^{2\alpha t}\right)t + \alpha^2\gamma^2\mathrm{e}^{3\alpha t}t^2\right)}{2\sqrt{\alpha\mathrm{e}^{3\alpha t}\sinh^3[\alpha t]\left(-2\alpha^2\left(\gamma^2t^2+2\right)+\left(4\alpha^2+\gamma^2\right)\cosh[2\alpha t]+\gamma^2\right)}}, \tag{5.11a}$$

$$\varphi_{12}(t) = -\frac{\sqrt{D}\gamma\mathrm{e}^{\alpha t}\left(\mathrm{e}^{2\alpha t}(2\alpha t-1)+1\right)}{2\sqrt{\alpha}\left(\mathrm{e}^{2\alpha t}-1\right)^{3/2}}, \tag{5.11b}$$

$$\varphi_{21}(t) = 0, \tag{5.11c}$$

$$\varphi_{22}(t) = \sqrt{\frac{\alpha D}{1-\mathrm{e}^{-2\alpha t}}}, \tag{5.11d}$$

and

$$\zeta_{11}(t) = \frac{\sqrt{D\left[\left(4\alpha^2+\gamma^2\right)\cosh(2\alpha t) - 2\alpha^2\left(\gamma^2t^2+2\right)-\gamma^2\right]}}{\alpha^{3/2}\sqrt{2(1-\mathrm{e}^{-2\alpha t})}}, \tag{5.12a}$$

$$\zeta_{12}(t) = 0, \tag{5.12b}$$

$$\zeta_{21}(t) = \frac{\gamma\sqrt{D}\left(2\alpha t - 1 + \mathrm{e}^{-2\alpha t}\right)}{2\alpha^{3/2}\sqrt{1-\mathrm{e}^{-2\alpha t}}}, \tag{5.12c}$$

https://doi.org/10.1017/jfm.2025.11092 Published online by Cambridge University Press

$$\zeta_{22}(t) = \sqrt{\frac{D}{\alpha}\left(1 - \mathrm{e}^{-2\alpha t}\right)}. \tag{5.12d}$$

With these source terms and the moment description (3.2) for an arbitrary initial condition, we obtain the following result:

$$\begin{aligned}\kappa_{11}(t) = {} & \kappa_{11}^0 \mathrm{e}^{2\alpha t} + \kappa_{12}^0 \frac{\gamma}{\alpha}\left(\mathrm{e}^{2\alpha t} - 1\right) + \kappa_{22}^0 \frac{\gamma^2}{\alpha^2} \sinh^2(\alpha t) + \frac{D}{\alpha}\left(\mathrm{e}^{2\alpha t} - 1\right) \\ & + \frac{D\gamma^2}{2\alpha^3} \sinh(2\alpha t) - \frac{D\gamma^2}{\alpha^2} t,\end{aligned} \tag{5.13a}$$

$$\kappa_{12}(t) = \kappa_{12}^0 + \kappa_{22}^0 \frac{\gamma}{2\alpha}\left(1 - \mathrm{e}^{-2\alpha t}\right) + \frac{D\gamma}{2\alpha^2}\left(2\alpha t + \mathrm{e}^{-2\alpha t} - 1\right), \tag{5.13b}$$

$$\kappa_{22}(t) = \kappa_{22}^0 \mathrm{e}^{-2\alpha t} + \frac{D}{\alpha}\left(1 - \mathrm{e}^{-2\alpha t}\right). \tag{5.13c}$$

These results reduce to the previous example in the limit $\alpha \to 0$. For $|\alpha| > 0$, the long-term scaling of the maximum concentration is exponential, $c_m(t) \propto 1/\sqrt{\det \kappa(t)} \propto \exp(-|\alpha| t)$. This result remains true for pure straining ($\gamma = 0$) and agrees with the lamella theory prediction (Villermaux 2019).

5.2. *Vortex flow*

Here we consider the idealised vortex flow discussed in Meunier & Villermaux (2003), given in polar coordinates by

$$\boldsymbol{u}(r, \theta) = \frac{\Gamma}{2\pi r} \boldsymbol{e}_\theta. \tag{5.14}$$

The only non-zero component of the strain-rate tensor (3.7) in the streamline coordinate system is $\epsilon_{12} = \gamma(r) \equiv \gamma(\boldsymbol{x}_0)$, where the radius of a streamline is also only dependent on the initial condition by virtue of (5.14). One thus has the relations

$$\gamma(r) = \frac{\Gamma}{\pi r^2} \equiv \gamma(\boldsymbol{x}_0) = \frac{\Gamma}{\pi |\boldsymbol{x}_0|^2}, \tag{5.15}$$

with

$$r = |\boldsymbol{x}_0|. \tag{5.16}$$

Thus, along a given streamline, characterised by constant radius r, the solute experiences constant shear only. The trajectories corresponding to initial locations $\boldsymbol{x}_0$ at time $t_0 = 0$ are given by

$$\boldsymbol{x}(t; \boldsymbol{x}_0) = r \cos[\theta(t; \boldsymbol{x}_0)] \boldsymbol{e}_1 + r \sin[\theta(t; \boldsymbol{x}_0)] \boldsymbol{e}_2, \tag{5.17}$$

with

$$\theta(t; \boldsymbol{x}_0) = \theta_0(\boldsymbol{x}_0) + \frac{\Gamma}{2\pi r^2} t\ , \qquad \theta_0(\boldsymbol{x}_0) = \mathrm{atan}(\mathrm{x}_{0,2}/\mathrm{x}_{0,1}). \tag{5.18}$$

According to (D5) the entries of $\boldsymbol{A}(t; \boldsymbol{x}_0)$ are defined by

$$\boldsymbol{v}(t; \boldsymbol{x}_0) = -\frac{\Gamma}{2\pi r} \sin[\theta(t; \boldsymbol{x}_0)] \boldsymbol{e}_1 + \frac{\Gamma}{2\pi r} \cos[\theta(t; \boldsymbol{x}_0)] \boldsymbol{e}_2, \tag{5.19}$$

https://doi.org/10.1017/jfm.2025.11092 Published online by Cambridge University Press

leading to

$$\boldsymbol{A}(t;\boldsymbol{x}_0)=\begin{bmatrix}-\sin\left[\theta_0(\boldsymbol{x}_0)+\Gamma t/\left(2\pi r^2\right)\right] & -\cos\left[\theta_0(\boldsymbol{x}_0)+\Gamma t/\left(2\pi r^2\right)\right]\\ \cos\left[\theta_0(\boldsymbol{x}_0)+\Gamma t/\left(2\pi r^2\right)\right] & -\sin\left[\theta_0(\boldsymbol{x}_0)+\Gamma t/\left(2\pi r^2\right)\right]\end{bmatrix}. \tag{5.20}$$

Since for each streamline we have constant shear, the entries of $\boldsymbol{\varphi}(t;\boldsymbol{x}_0)$ and $\boldsymbol{\zeta}(t;\boldsymbol{x}_0)$ are the same as those for shear flow, so that they are given by (5.2) and (5.3) with γ given by (5.15). This yields

$$\begin{aligned}&\varphi_{11}(t;\boldsymbol{x}_0)=\frac{\sqrt{3}D\left(\Gamma^2t^2+4\pi r^4\right)}{2\pi r^2\sqrt{2D\Gamma^2t^3+24Dt\pi r^4}}, && \varphi_{12}(t;\boldsymbol{x}_0)=-\frac{\Gamma\sqrt{Dt}}{2\pi r^2\sqrt{2}},\\ &\varphi_{21}(t;\boldsymbol{x}_0)=0, && \varphi_{22}(t;\boldsymbol{x}_0)=\sqrt{\frac{D}{2t}},\end{aligned} \tag{5.21}$$

and

$$\begin{aligned}&\zeta_{11}(t;\boldsymbol{x}_0)=\sqrt{2Dt+\frac{D\Gamma^2t^3}{6\pi r^4}}, && \zeta_{12}(t;\boldsymbol{x}_0)=0,\\ &\zeta_{21}(t;\boldsymbol{x}_0)=\frac{\Gamma t\sqrt{2Dt}}{2\pi r^2}, && \zeta_{22}(t;\boldsymbol{x}_0)=\sqrt{2Dt};\end{aligned} \tag{5.22}$$

recall (5.16).

The characteristic lines in the streamline coordinate frame are given according to (3.15) as

$$\hat{\boldsymbol{z}}(t;\boldsymbol{\xi},\boldsymbol{z}_0)=\begin{bmatrix}z_{0,1}+\dfrac{\Gamma z_{0,2}}{\pi r^2}t+\xi_1\sqrt{2Dt+\dfrac{D\Gamma^2t^3}{6\pi r^4}}+\xi_2\dfrac{\Gamma t\sqrt{2Dt}}{2\pi r^2}\\ z_{0,2}+\xi_2\sqrt{2Dt}\end{bmatrix}. \tag{5.23}$$

The forward map (4.1) of support particles can be obtained explicitly by combining (5.17), (5.20) and (5.22) (not shown for brevity). The backward map $\hat{\boldsymbol{x}}_0$ for an arbitrary point can be similarly obtained from (4.6) given the matrix $\boldsymbol{B}(t;\boldsymbol{x}_0)$, which according to (3.16) is

$$\boldsymbol{B}(t;\boldsymbol{x}_0)=\begin{bmatrix}1 & \dfrac{\Gamma}{\pi r^2}t\\ 0 & 1\end{bmatrix}. \tag{5.24}$$

For a given initial condition, using the analytical expressions (5.14)–(5.24), the normalised concentration field can be explicitly computed for a Lagrangian unstructured grid using (4.4) or an imposed grid using (4.7).

Numerical algorithms based on the concept of lamellae have been constructed to consider initial concentration profiles that are symmetric along the transversal direction of the lamellae and constant along the longitudinal direction (Meunier & Villermaux 2010; Martínez-Ruiz *et al.* 2018; Sen *et al.* 2020; Meunier & Villermaux 2022; Pushenko *et al.* 2025). Additionally, lamella models neglect diffusion along lamellae, a mechanism that can be important at long times or low Péclet numbers. These approximations are not needed in the present framework. To illustrate this, we introduce uniform, normal and skew-normal distributions:

https://doi.org/10.1017/jfm.2025.11092 Published online by Cambridge University Press

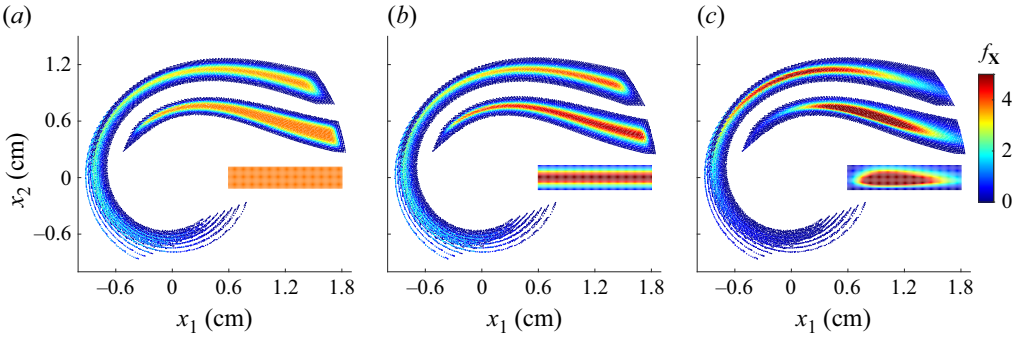


Figure 3. Temporal evolution of solute plumes in a vortex flow defined by (*a*) a uniform initial profile (5.27*a*), (*b*) a uniform-normal initial profile (5.27*b*) and (*c*) a skewed initial profile (5.27*c*) at $t = 0$ s, $t = 0.35$ s and $t = 0.8$ s. Based on the set-up of Meunier & Villermaux (2003), we set $a_1 = 0.6$ cm, $b_1 = 1.8$ cm, $a_2 = -0.11$ cm, $b_2 = 0.11$ cm, $\Gamma = 14.2$ cm^2 s^{-1} and we take $D = 10^{-3}$ cm^{2}s^{-1} as an intermediate value from those used in Meunier & Villermaux (2010), which corresponds to $Pe_{\tilde{\gamma}} \approx 6 \times 10^2$. The Lagrangian grids correspond to support particle locations with a uniform discretisation of $\boldsymbol{x}_0$ and $\boldsymbol{\xi}$.

$$f_{\mathcal{U}}(x; a, b) = \frac{\mathcal{H}(x-a)\mathcal{H}(b-x)}{b-a}, \tag{5.25a}$$

$$f_{\mathcal{N}}(x; \mu, \sigma) = \frac{1}{\sqrt{2\pi}\sigma} \exp\left[-\frac{(x-\mu)^2}{2\sigma^2}\right], \tag{5.25b}$$

$$f_{\mathcal{S}}(x; \mu, \sigma, \alpha) = \omega^{-1} f_{\mathcal{N}}((x-\eta)/\omega; 0, 1)\big(1 + \mathrm{erf}\big[\alpha(x-\eta)/(\omega\sqrt{2})\big]\big). \tag{5.25c}$$

Here $\mathcal{H}(\cdot)$ denotes the Heaviside function and

$$\omega = \frac{\sigma}{\sqrt{1 - 2\delta^2/\pi}}, \qquad \eta = \mu - \omega\delta\sqrt{2/\pi}, \qquad \delta = \frac{\alpha}{\sqrt{1+\alpha^2}}. \tag{5.26}$$

Then, we combine these shapes along the two Cartesian directions to form three example initial conditions:

$$f_{\boldsymbol{X}}^{0\mathcal{U}}(\boldsymbol{x}) = f_{\mathcal{U}}(x_1; a_1, b_1) f_{\mathcal{U}}(x_2; a_2, b_2), \tag{5.27a}$$

$$f_{\boldsymbol{X}}^{0\mathcal{UN}}(\boldsymbol{x}) = f_{\mathcal{U}}(x_1; a_1, b_1) f_{\mathcal{N}}(x_2; \mu_2, \sigma_2), \tag{5.27b}$$

$$f_{\boldsymbol{X}}^{0\mathcal{S}}(\boldsymbol{x}) = f_{\mathcal{S}}(x_1; \mu_1, \sigma_1, 4) f_{\mathcal{S}}(x_2; \mu_2, \sigma_2, 4). \tag{5.27c}$$

For comparison purposes, we choose the first two moments of all initial conditions along both Cartesian directions to be the same by imposing $\mu_1 = (a_1 + b_1)/2$, $\mu_2 = (a_2 + b_2)/2$, $\sigma_1 = (b_1 - a_1)/\sqrt{12}$ and $\sigma_2 = (b_2 - a_2)/\sqrt{12}$, and we define the width as $s_0 = b_2 - a_2$ and the length as $l_0 = b_1 - a_1$ based on the uniform initial condition (5.27*a*). Note that the initial condition (5.27*a*) corresponds to the case in Meunier & Villermaux (2003) and (5.27*b*) to Meunier & Villermaux (2010) and Sen *et al.* (2020). Concentration profiles for these three initial conditions are compared in figure 3. To highlight the fact that the hyperbolic formulation introduced here allows for choosing the spatial locations where one wishes to compute the concentration profile at a given time, we also depict the evolution of the skewed concentration profile (5.27*c*) for different grid choices in figure 4. In particular, Lagrangian grids composed by the positions of support particles (as in figure 3) are shown in figure 4(*a–c*) at different resolutions; uniform grids are shown in panels (*d–f*) and three arbitrary unstructured grids are shown in panels (*g–i*).

https://doi.org/10.1017/jfm.2025.11092 Published online by Cambridge University Press

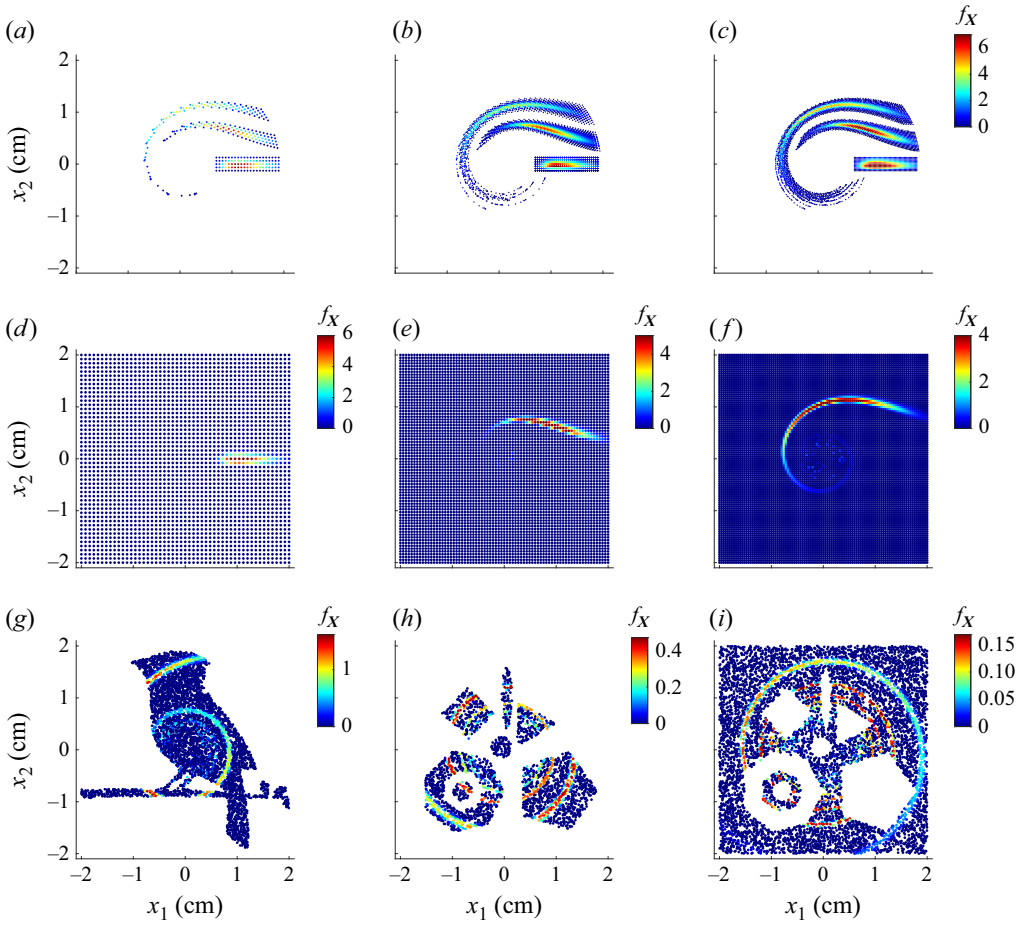


Figure 4. Temporal evolution of the skewed concentration profile (5.27*c*) for different grid types. Top row: concentration profiles at $t = 0$ s, $t = 0.35$ s and $t = 0.8$ s for an initially uniform Lagrangian grid composed of support particles with three levels of refinement: (*a*) coarse, (*b*) medium and (*c*) fine. Middle row: concentration profiles for three uniform grids with different levels of refinement: (*d*) coarse at $t = 0$ s, (*e*) medium at $t = 0.35$ s and (*f*) fine at $t = 0.8$ s. Bottom row: arbitrary unstructured grids are employed to depict the solution at (*g*) $t = 2$ s, (*h*) $t = 5$ s and (*i*) $t = 10$ s. The rest of the parameters are given in the caption of figure 3.

To further quantify the influence of radial diffusion on mixing in a vortex, we consider the maximum concentration $c_m(r, t)$ profile as a function of radial position and time both considering diffusion in all directions and neglecting radial diffusion. As we will see, local linearisation of the flow affects the results at late times. We begin by discussing the linearised behaviour and consider its role below. We focus on initial conditions (5.27*a*) and (5.27*b*), for which the calculations can be carried out analytically. Because the Jacobian of the transformation (2.8*a*) is unity, $J(t) = 1$, and the domain is unbounded, concentration gradients cannot grow over time. This holds for incompressible flows with a constant diffusion coefficient by virtue of (2.8*b*). Thus, the maximum radial concentration profile for a symmetric initial condition with respect to the x_1 axis will travel along those streamlines that at the initial time start along the line $x_2 = 0$.

To describe the maximum concentration profile at time t, consider a position $\boldsymbol{x}_m(r, t)$ such that $|\boldsymbol{x}_m(r, t)| = r$. Since the flow has no radial component, this position corresponds

https://doi.org/10.1017/jfm.2025.11092 Published online by Cambridge University Press

to a maximum if and only if the backward flow map associates it with the position $\hat{\boldsymbol{x}}_0[\boldsymbol{x}_m(r,t),t]=(r,0)^\top$ at the initial time; see (4.5). We first obtain the backward map in the streamline coordinate system for a given point $\boldsymbol{x}$ that at time t coincides with the streamline, i.e. taking $\boldsymbol{z}=\boldsymbol{0}$ in (3.18). We find that

$$\hat{\boldsymbol{z}}_0[\boldsymbol{\xi},\boldsymbol{x}_m(r,t),t]=\begin{bmatrix}\xi_2\dfrac{\Gamma t\sqrt{2Dt}}{2\pi r^2}-\xi_1\sqrt{2Dt+\dfrac{D\Gamma^2t^3}{6\pi^2r^4}}\\ -\xi_2\sqrt{2Dt}\end{bmatrix}, \tag{5.28}$$

where $r=|\boldsymbol{x}|=|\hat{\boldsymbol{x}}_0(\boldsymbol{x},t)|$. The full backward map in the Cartesian frame is (see Appendix E)

$$\hat{\boldsymbol{x}}_0(\boldsymbol{\xi},\boldsymbol{x},t)=\hat{\boldsymbol{x}}_0(\boldsymbol{x},t)+\boldsymbol{A}\big[0;\hat{\boldsymbol{x}}_0(\boldsymbol{x},t)\big]\hat{\boldsymbol{z}}_0(\boldsymbol{\xi},\boldsymbol{x},t), \tag{5.29}$$

which combined with (5.28) gives

$$\hat{\boldsymbol{x}}_0[\boldsymbol{\xi},\boldsymbol{x}_m(r,t),t]=\left(r+\xi_2\sqrt{2Dt}\right)\boldsymbol{e}_1+\left(\xi_2\frac{\Gamma t\sqrt{2Dt}}{2\pi r^2}-\xi_1\sqrt{2Dt+\frac{D\Gamma^2t^3}{6\pi^2r^4}}\right)\boldsymbol{e}_2. \tag{5.30}$$

Consider now what happens if we neglect radial diffusion. The second component of (5.28) represents deviations in the initial condition along the radial direction, because it is locally perpendicular to the flow direction. If no radial diffusion is present, no radial deviations can occur when tracing backward. Specifically, this corresponds to neglecting the noise contribution along the second component of the characteristic lines in the streamline coordinate system. That is, taking $[\boldsymbol{\zeta}^\top(t)\boldsymbol{\xi}]_2=0$ (and $\boldsymbol{z}=\boldsymbol{0}$ as before) in (3.18) leads to

$$\hat{\boldsymbol{z}}_0[\boldsymbol{\xi},\boldsymbol{x}_m(r,t),t]=\begin{bmatrix}\xi_2\dfrac{\Gamma t\sqrt{2Dt}}{2\pi r^2}-\xi_1\sqrt{2Dt+\dfrac{D\Gamma^2t^3}{6\pi^2r^4}}\\ 0\end{bmatrix}, \tag{5.31}$$

from which

$$\hat{\boldsymbol{x}}_0[\boldsymbol{\xi},\boldsymbol{x}_m(r,t),t]=r\boldsymbol{e}_1+\left(\xi_2\frac{\Gamma t\sqrt{2Dt}}{2\pi r^2}-\xi_1\sqrt{2Dt+\frac{D\Gamma^2t^3}{6\pi^2r^4}}\right)\boldsymbol{e}_2. \tag{5.32}$$

Considering the uniform initial condition (5.27*a*), relation (4.7) together with (5.30) yields the maximum concentration profile

$$\begin{aligned}\frac{c_m(r,t)}{c_0}=\frac{f_X[\boldsymbol{x}_m(r,t);t]}{\max_{\boldsymbol{x}}[f_X(\boldsymbol{x};0)]}&=\mathcal{B}\left(k_2,\frac{-a}{\sqrt{b^2+1}};\frac{-b}{\sqrt{b^2+1}}\right)-\mathcal{B}\left(k_1,\frac{-a}{\sqrt{b^2+1}};\frac{-b}{\sqrt{b^2+1}}\right)\\&+\mathcal{B}\left(k_2,\frac{a}{\sqrt{b^2+1}};\frac{-b}{\sqrt{b^2+1}}\right)-\mathcal{B}\left(k_1,\frac{a}{\sqrt{b^2+1}};\frac{-b}{\sqrt{b^2+1}}\right),\end{aligned} \tag{5.33}$$

in terms of the bivariate normal cumulative distribution according to Owen (1980):

$$\mathcal{B}(\mathrm{k}_1,\mathrm{k}_2;\rho)=\frac{1}{2\pi\sqrt{1-\rho^2}}\int_{-\infty}^{\mathrm{k}_2}\mathrm{d}y\int_{-\infty}^{\mathrm{k}_1}\mathrm{d}x\ \exp\left[-\frac{x^2-2\rho xy+y^2}{2(1-\rho^2)}\right], \tag{5.34}$$

https://doi.org/10.1017/jfm.2025.11092 Published online by Cambridge University Press

with

$$a = \frac{\pi s_0}{2\sqrt{D\left(\frac{\Gamma^2 t^3}{6r^4} + 2\pi^2 t\right)}}, \qquad b = \frac{\sqrt{3}\Gamma t}{\sqrt{\Gamma^2 t^2 + 12\pi^2 r^4}},$$
$$k_1 = \frac{r - a_1}{\sqrt{2Dt}}, \qquad k_2 = \frac{b_1 - r}{\sqrt{2Dt}}, \tag{5.35}$$

where c_0 is the initial maximum concentration anywhere in the domain. If we neglect radial diffusion, combining (4.7) and (5.32) gives

$$\frac{c_m(r,t)}{c_0} = \operatorname{erf}\left[\frac{\sqrt{3}\pi s_0 r^2}{4\sqrt{Dt\left(3\pi^2 r^4 + \Gamma^2 t^2\right)}}\right]\mathcal{H}[r - a_1]\mathcal{H}[b_1 - r]. \tag{5.36}$$

This coincides with the result in Meunier & Villermaux (2003) obtained under this approximation. The difference between (5.33) and (5.36) can be clearly seen in figure 5(*c*). To understand when significant differences occur, consider the strip Péclet number based on the second moment σ_1^2 of the initial condition along the radial direction, $Pe_{\tilde{\gamma}} = \tilde{\gamma}\sigma_1^2/D$, where $\tilde{\gamma}$ is the average shear over the initial condition. We have $\tilde{\gamma} \approx \Gamma(a_1^{-1} - b_1^{-1})/\pi$ provided that $s_0 \ll l_0$, obtained by averaging (5.15) over $a_1 \leqslant r \leqslant b_1$. The strip Péclet number for the results in figure 5(*a–c*) has values $Pe_{\tilde{\gamma}} = 10^5$, 6×10^3 and 60. Diffusion along the radial direction becomes important for times of the order of the time scale $\tau_D = \sigma_1^2/D$ (Dentz *et al.* 2018). For the final time in figure 5, $t = 20$ s, we find that $t/t_D = 0.42$ (*a*), 0.83 (*b*) and 1.67 (*c*).

Proceeding the same way for the uniform-normal initial condition (5.27*b*), the maximum concentration profile considering diffusion in all directions is

$$\frac{c_m(r,t)}{c_0} = \frac{\pi s_0 r^2}{2\sqrt{8D\Gamma^2 t^3 + \pi^2 r^4\left(s_0^2 + 24Dt\right)}}\left(\operatorname{erf}\left[\frac{b_1 - r}{\mathrm{q}(r,t)}\right] - \operatorname{erf}\left[\frac{a_1 - r}{\mathrm{q}(r,t)}\right]\right), \tag{5.37a}$$

$$\mathrm{q}(r,t) = 2\sqrt{Dt - \frac{6D\Gamma^2 t^4}{8\Gamma^2 t^3 + \pi^2 r^4\left(s_0^2/D + 24t\right)}}, \tag{5.37b}$$

and neglecting radial diffusion, we find that

$$\frac{c_m(r,t)}{c_0} = \frac{\pi s_0 r^2}{\sqrt{8D\Gamma^2 t^3 + \pi^2 r^4\left(s_0^2 + 24Dt\right)}}\mathcal{H}[r - a_1]\mathcal{H}[b_1 - r]. \tag{5.38}$$

These results are depicted in figure 5(*d–f*) for different values of the diffusion coefficient at three different times. The values of the strip Péclet number and times are the same as for figure 5(*a–c*) and, for the same reason as before, the difference between these solutions is mainly visible in figure 5(*f*). The solutions for the uniform initial condition considered above are also shown, highlighting the importance of the initial condition even at times $t > \tau_D$.

The shape of the initial condition does not influence the asymptotic scaling of the decay of the maximum concentration, although the value of the maximum concentration at a given time depends on the initial condition. Neglecting radial diffusion, on the other hand, does affect the asymptotic scaling. To quantify this, denote by $r_m(t)$ the radius where the maximum concentration occurs for a given time, for which an implicit relation may be

https://doi.org/10.1017/jfm.2025.11092 Published online by Cambridge University Press

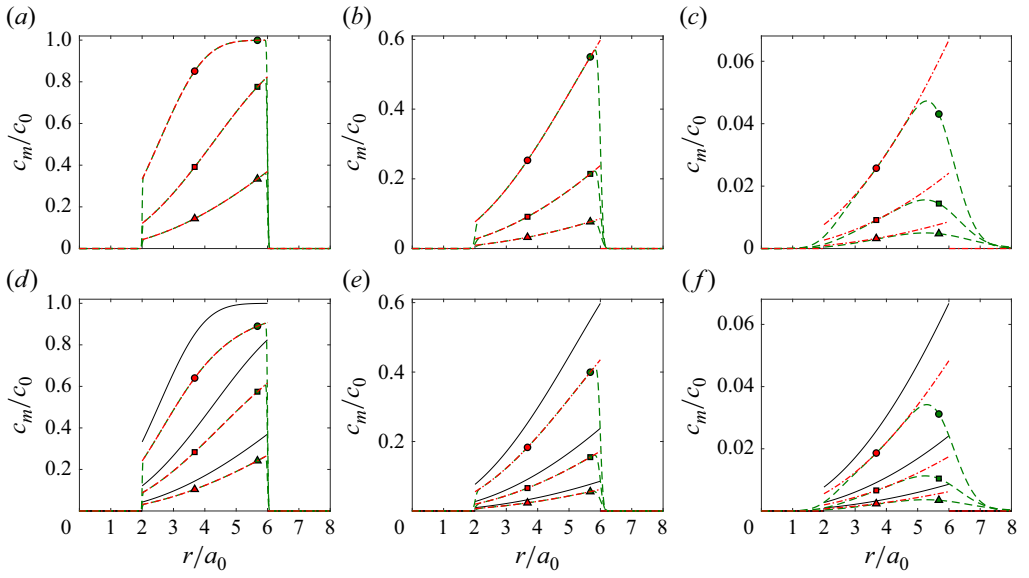


Figure 5. Maximum concentration along the radial direction for the uniform initial condition (5.27*a*) in (*a–c*) and the uniform-normal initial condition (5.27*b*) in (*d–f*) at times $t = 5$ s (circles), $t = 10$ s (squares), $t = 20$ s (triangles) with $D = 5 \times 10^{-6}$ cm^2 s^{-1} ($Pe_{\tilde{\gamma}} \approx 10^5$) in (*a*) and (*d*); $D = 10^{-4}$ cm^2 s^{-1} ($Pe_{\tilde{\gamma}} \approx 6 \times 10^3$) in (*b*) and (*e*); and $D = 10^{-2}$ cm^2 s^{-1} ($Pe_{\tilde{\gamma}} \approx 60$) in (*c*) and (*f*). The dash-dotted red lines in (*a–c*) are (5.36) and in (*d–f*) they are (5.38); whereas the dashed green lines in (*a–c*) are (5.33) and in (*d–f*) they are (5.37*a*). The continuous black lines in (*d–f*) are (5.36). The radius is normalised by the initial vortex radius $a_0 = 0.3$ cm (Meunier & Villermaux 2003). The remaining parameters are as in figure 3. The green curves consider radial diffusion, whereas the red and black curves do not.

found using (5.33) and (5.37*a*) for the initial conditions (5.27*a*) and (5.27*b*), respectively. For sufficiently long times, the maximum concentration anywhere in the domain evolves as $c_m(t) = c_m[r_m(t), t] \propto t^{-2}$. If radial diffusion is neglected, the maximum concentration occurs at the maximum radius, i.e. one simply has $r_m(t) = b_1$ for all times from (5.36) and (5.38). Considering the uniform-normal initial condition (5.27*b*), and neglecting the influence of radial diffusion, the maximum concentration profile at long times according to (5.38) evolves as $c_m(t) \propto t^{-3/2}$ instead of t^{-2}. The same is true for the uniform initial condition (5.27*a*) according to (5.36), making use of $\mathrm{erf}(x) \approx 2x/\sqrt{\pi}$ for $x \ll 1$.

The nonlinearity of the flow (5.14) restricts the validity of the scalings of the maximum concentration derived above to times shorter than the diffusion time, regardless of the Péclet number and the consideration of radial diffusion. After the combination of stretching and diffusion has homogenised the plume in the radial support $a_1 \lesssim r \lesssim b_1$, the solute forms an axisymmetric annular-shaped profile. This is accompanied by an abrupt change in the scaling of the maximum concentration. Eventually, a disk-shaped plume is formed, leading to a pure diffusion regime along the radial direction, characterised by a scaling $c_m(t) \propto t^{-1}$.

Figure 6(*a–e*) shows the time evolution of the solute plume computed with the relinearisation procedure proposed in § 4. The behaviour of the maximum concentration with and without relinearisation is shown in figure 6(*f*) and compared with the solution obtained from a standard finite-difference PDE solver, using second-order central discretisation in space and a total variation diminishing, third-order Runge–Kutta method in time (Gottlieb & Shu 1998). The late-time dynamics of the concentration field is governed by the nonlinearities in the flow, which are only correctly captured if

https://doi.org/10.1017/jfm.2025.11092 Published online by Cambridge University Press

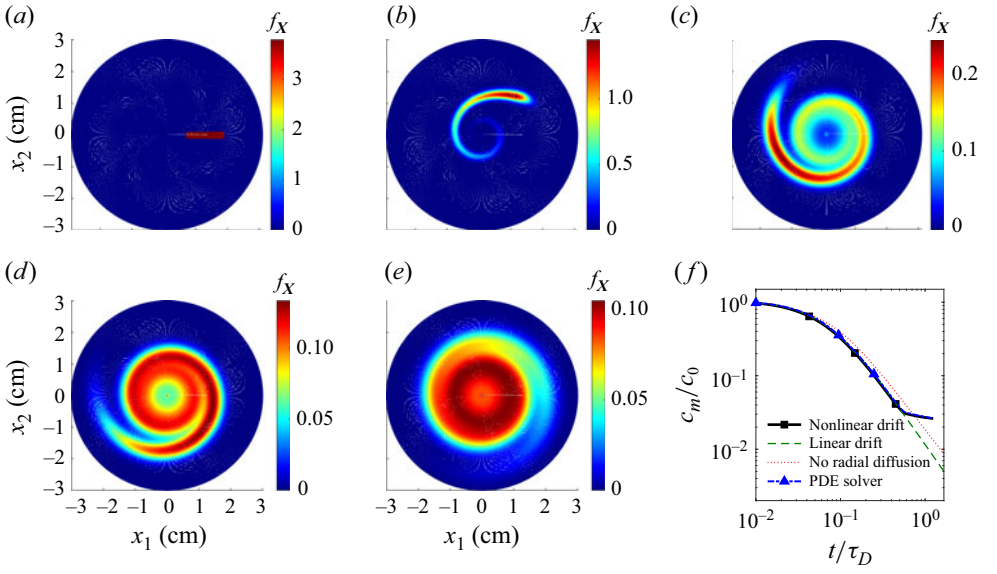


Figure 6. Time evolution of the uniform initial condition (5.25*a*) for $D = 10^{-2}$ cm^2 s^{-1}, which corresponds to $Pe_{\tilde{y}} \approx 60$ at (*a*) $t = 0$ s, (*b*) $t = 1$ s, (*c*) $t = 4$ s, (*d*) $t = 6$ s and (*e*) $t = 10$ s computed with the relinearisation procedure with a linear interpolant with nodes distributed uniformly in polar coordinates (with 301×601 points in the radial and azimuthal directions, respectively) for a radial domain of $r \in [0, 3]$ cm and the full circumference. Relinearisation is applied at intervals of $\Delta t = 0.02$ s. Panel (*f*) shows the maximum concentration assuming linearity of the drift and neglecting radial diffusion using (5.36) (dotted red line), assuming linearity of the drift but considering radial diffusion with (5.33) (dashed green line), using the relinearisation procedure while accounting for radial diffusion (continuous black line with squared symbols) and using the PDE solver in a $[-3, 3] \times [-3, 3]$ cm^2 domain discretised in 401×401 points with a time step of $\Delta t = 6 \times 10^{-5}$ s (dot-dashed blue line with triangular symbols).

relinearisation is applied. It should be noted that (5.14) is a simplification of the Lamb–Oseen vortex model that is accurate far from the vortex core (Meunier & Villermaux 2003). We restrict the time frame in figure 6(*f*) such that the maximum of the solute plume is far from the centre, so that the artificial singularity at $r = 0$ does not affect the results significantly. Correspondingly, we limit the velocities in the finite-difference solver to the value at $r = 0.05$ cm. For this reason, the $c_m(t) \propto t^{-1}$ scaling expected for a radially diffusing, disk-shaped plume cannot be observed cleanly under this model.

5.3. *Bidimensional heterogeneous Darcy flow*

Here we consider the evolution of the concentration profile of a solute in a heterogeneous porous medium. In particular, we compare the hyperbolic formulation with the particle tracking simulations based on the Langevin system (2.3) with the concentration profile reconstructed according to a discretised version of (2.4) using square bins.

We consider a Darcy (continuum) scale, steady-state velocity field $\boldsymbol{u}(\boldsymbol{x})$ described by the Darcy equation (Bear 1972),

$$\boldsymbol{u}(\boldsymbol{x}) = -K(\boldsymbol{x})\nabla \mathrm{h}(\boldsymbol{x}), \tag{5.39}$$

where $K(\boldsymbol{x})$ is the (isotropic) hydraulic conductivity and $\mathrm{h}(\boldsymbol{x})$ the hydraulic head. We take the flow field to be incompressible, such that the continuity equation reads $\nabla \cdot \boldsymbol{u} = 0$,

https://doi.org/10.1017/jfm.2025.11092 Published online by Cambridge University Press

leading to an explicit equation for the hydraulic head field,

$$\nabla \cdot K(\boldsymbol{x})\nabla \mathrm{h}(\boldsymbol{x}) = 0. \tag{5.40}$$

We take $K(\boldsymbol{x})$ as a single realisation of a random field such that the log-conductivity field, $f(\boldsymbol{x}) = \ln[K(\boldsymbol{x})/K_0]$, with K_0 an arbitrary reference permeability, has a log-Gaussian point distribution, ensemble mean μ_f, ensemble variance σ_f^2 and Gaussian spatial correlation structure with isotropic correlation length l_c. Since the correlation length l_c provides a characteristic spatial length scale, it is convenient to introduce a Péclet number $Pe = \overline{u} l_c/D$, where $\overline{u}$ is the magnitude of the average of the Darcy velocity field (5.39) and D is the dispersion coefficient. We have $Pe = \tau_D/\tau_A$, where $\tau_D = \ell_c^2/D$ and $\tau_A = \ell_c/\overline{u}$ are the diffusion and advection time scales associated with this length scale. We normalise lengths by ℓ_c, times by τ_A and velocities by $\overline{u}$, so that, due to linearity of the flow, the numerical values of these quantities do not play a role and we work with non-dimensional magnitudes t/τ_A, $\boldsymbol{x}/l_c$ and $\boldsymbol{u}/\overline{u}$. Then, the flow field is obtained for a permeability field realisation with $\mu_f = 1$ and $\sigma_f^2 = 1/4$, and an imposed mean Darcy flow velocity aligned with the horizontal direction. To generate the permeability field and compute the flow field, we make use of the freely available solver developed in Zhou & Hansen (2022, 2024). The permeability field is computed using a spectral approach and the flow is solved in a uniform grid using a finite volume method in terms of interfacial Darcy fluxes by combining (5.39) and (5.40) in integral form. We consider a bidimensional domain of 25×100 correlation lengths along the horizontal and vertical directions, respectively, with periodic boundary conditions and discretised in 20 cells per correlation length along each direction. A third-order interpolant is then used to compute the resulting flow field at arbitrary locations. For transport, the Péclet number is set by varying the value of the diffusion coefficient D. We consider times up to $t_{end} = 60\tau_A$ and Péclet numbers $Pe = 10^3$ and 10^4. These times are small compared with τ_D, respectively $t_{end}/\tau_D = 6 \times 10^{-2}$ and 6×10^{-3}, and we do not apply the relinearisation procedure proposed in § 4 here.

Because they are commonly employed and play an important role in theoretical and practical applications, as well as to illustrate certain advantages of the formulation introduced here, we focus on singular initial conditions, characterised by the presence of infinite spatial gradients. In particular, we consider the point and line initial injections

$$f_{\boldsymbol{X}}^{p}(\boldsymbol{x}; \boldsymbol{a}) = \delta(\boldsymbol{x} - \boldsymbol{a}), \tag{5.41a}$$

$$f_{\boldsymbol{X}}^{l}(\boldsymbol{x}; \boldsymbol{b}) = \frac{\mathcal{H}(x_2 - b_1)\mathcal{H}(b_2 - x_2)}{b_2 - b_1}\delta(x_1 - b_3), \tag{5.41b}$$

at the location $\boldsymbol{x} = \boldsymbol{a}$ and along the line $b_1 \leqslant x_2 \leqslant b_2$ and $x_1 = b_3$. respectively. In the numerical examples below, we take $\boldsymbol{a}/l_c = (2, 12.5)^\top$ for (5.41*a*) and $\boldsymbol{b}/l_c = (8.5, 16.5, 2)^\top$ for (5.41*b*). Note that the strip Péclet number along degenerate (zero-width) directions of the initial condition has zero width. These types of initial conditions present numerical difficulties for Eulerian treatments of the FPE (2.2*a*), because regularisation of the Dirac delta and Heaviside functions is required (Suarez, Jacobs & Don 2014; Suarez & Jacobs 2017; Wissink *et al.* 2018; Domínguez-Vázquez *et al.* 2021). Particle tracking simulations, on the other hand, are easily applicable for these initial conditions. However, the reconstruction of the PDF $f_{\boldsymbol{X}}$ is sensitive to the coexistence of spatial scales with large disparity on the solute plume, which complicates the search for an optimal bandwidth in case of the use of kernel density estimators, or bin size in the case of histograms. As a consequence, practical implementations of the reconstruction (2.4) introduce errors that are hard to estimate without the knowledge of the true (unknown) concentration profile. It is not the intention of this paper to use state-of-the-art kernel density estimators for

https://doi.org/10.1017/jfm.2025.11092 Published online by Cambridge University Press

reconstructing the particle PDF $f_{\boldsymbol{X}}$ (Fernàndez-Garcia & Sánchez-Vila 2011; Pedretti & Fernàndez-Garcia 2013; Sole-Mari *et al.* 2019; Benson *et al.* 2021). Instead, we use histograms to reconstruct $f_{\boldsymbol{X}}$ from Monte Carlo computations of (2.3) using the Euler-Maruyama method, in order to compare and validate the proposed formulation. This way, we eliminate additional intricacies related to PDF reconstruction and focus on the illustration of some of the advantages of the hyperbolic formulation, such as its ability to handle singular profiles, targeting locations of interest and reducing the computational cost. All particle tracking results in this section employ $N = 10^6$ particles.

Now we proceed to describe the evolution of the PDF of solute particle locations with relations (4.6) and (4.7). We look at an arbitrary point $\boldsymbol{x}$ at time t, such that the backward flow map is $\hat{\boldsymbol{x}}_0(\boldsymbol{x}, t) = \boldsymbol{x}(0; \boldsymbol{x}, t)$. Then, we define the matrix

$$\boldsymbol{P}[t; \boldsymbol{x}] = \boldsymbol{A}\big[0; \hat{\boldsymbol{x}}_0(\boldsymbol{x}, t)\big]\boldsymbol{B}\big[t; \hat{\boldsymbol{x}}_0(\boldsymbol{x}, t)\big]^{-1}\boldsymbol{\zeta}\big[t; \hat{\boldsymbol{x}}_0(\boldsymbol{x}, t)\big]^{\top}, \tag{5.42}$$

and from (4.6) the backward map is simply

$$\hat{\boldsymbol{x}}_0(\boldsymbol{\xi}, \boldsymbol{x}, t) = \hat{\boldsymbol{x}}_0(\boldsymbol{x}, t) - \boldsymbol{P}[t; \boldsymbol{x}]\boldsymbol{\xi}. \tag{5.43}$$

Finally, combining (5.43) with (4.7) and making use of the Dirac-delta properties, one can obtain for the initial condition (5.41*a*), the PDF of solute particle locations:

$$f_{\boldsymbol{X}}(\boldsymbol{x}; t) = \frac{\exp\left[-\frac{1}{2}\left(\hat{\boldsymbol{x}}_0(\boldsymbol{x}, t) - \boldsymbol{a}\right)^{\top}\left(\boldsymbol{P}[t; \boldsymbol{x}]^{\top}\boldsymbol{P}[t; \boldsymbol{x}]\right)^{-1}\left(\hat{\boldsymbol{x}}_0(\boldsymbol{x}, t) - \boldsymbol{a}\right)\right]}{2\pi\,\det(\boldsymbol{P}[t; \boldsymbol{x}])}. \tag{5.44}$$

This is a semi-analytic result, in the sense that once the matrix $\boldsymbol{P}$ and the initial position $\hat{\boldsymbol{x}}_0$ according to the backward flow map are known, the concentration field follows analytically. Because of the spatial dependence of the velocity field, these two quantities are to be calculated numerically using standard ODE solvers along streamlines. If we repeat the same procedure for (5.41*b*), using the properties of both the Dirac delta and Heaviside functions, we find that

$$f_{\boldsymbol{X}}(\boldsymbol{x}; t) = \frac{\exp\left(-\mathrm{C}^2[b_3]\right)}{\sqrt{8\pi\left(P_{11}^2 + P_{12}^2\right)}}\frac{\mathrm{erf}\left(\mathrm{D}[b_3] - \mathrm{E}[b_1]\right) - \mathrm{erf}\left(\mathrm{D}[b_3] - \mathrm{E}[b_2]\right)}{b_2 - b_1}, \tag{5.45a}$$

$$\mathrm{C}[b] = \frac{b - \hat{\mathrm{x}}_{0,1}}{\sqrt{2\left(P_{11}^2 + P_{12}^2\right)}}, \quad \mathrm{D}[b] = \frac{P_{11}P_{21} + P_{12}P_{22}}{\det(\boldsymbol{P})}\mathrm{C}[b], \tag{5.45b}$$

$$\mathrm{E}[b] = \frac{b - \hat{\mathrm{x}}_{0,2}}{\det(\boldsymbol{P})}\sqrt{\frac{P_{11}^2 + P_{12}^2}{2}}, \tag{5.45c}$$

where we have omitted the arguments of $\boldsymbol{P}$, its matrix elements P_{ij} and backward flow map components $\hat{\mathrm{x}}_{0,i}$ for brevity.

For the point-based injection (5.41*a*), we illustrate the method by tracing the evolution of the PDF $f_{\boldsymbol{X}}$ along the corresponding streamline, $\boldsymbol{x}(t; \boldsymbol{a})$, demonstrating the ability of the hyperbolic formulation to target particular locations of interest. This is shown in figure 7(*a*) for $Pe = 10^4$ and figure 7(*b*) for $Pe = 10^3$, along with the classical particle tracking solutions for the concentration profile. The background shows the permeability field and a quiver plot of the flow field.

By interpolating the PDF $f_{\boldsymbol{X}}$ at the location of the trajectory for any given time, both approaches can be compared more directly, as shown in figure 8. It should be noted that the optimal bin size (or kernel bandwidth) for reconstructing the particle

https://doi.org/10.1017/jfm.2025.11092 Published online by Cambridge University Press

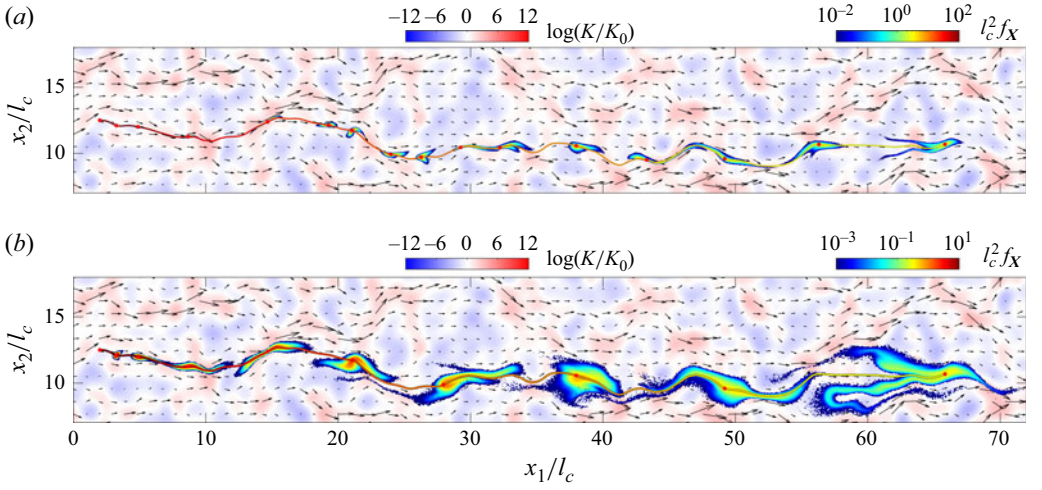


Figure 7. Evolution of the PDF of solute particle positions f_X in a heterogeneous medium for the initial condition (5.41*a*) for Péclet number s (*a*)$Pe = 10^4$ and (*b*) $Pe = 10^3$. The plots show the PDF reconstructed from Monte Carlo particle tracking simulations using histograms with bin side (*a*) $h = l_c/50$ and (*b*) $h = l_c/20$ for several times (contour maps), and the evolution of the PDF along the locations of the particle trajectory starting at $x_{0,1} = a_1$, $x_{0,2} = a_2$ (coloured continuous line) computed with (5.44).

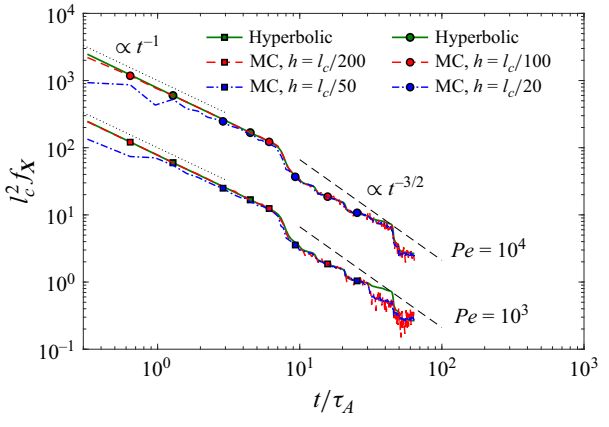


Figure 8. Evolution of the maximum of the PDF of solute particle positions f_X in a heterogeneous medium for the initial condition (5.41*a*), computed with the hyperbolic formulation (5.44) (continuous lines) and reconstructed from Monte Carlo particle tracking simulations with finer (dashed lines) and coarser (dash-dotted lines) histogram bin sizes. Monte Carlo results are also interpolated at the location of the trajectory from figure 7 with a zeroth-order interpolation for Péclet numbers $Pe = 10^3$ (squares) and $Pe = 10^4$ (circles). The tendencies shown correspond to the analysis in Dentz *et al.* (2018).

tracking PDF depends non-trivially on time, space and the Péclet number, complicating the reconstruction of the PDF from particle tracking simulations. Whist it is beyond the scope of the present work to assess state-of-the-art reconstruction techniques, which can improve the particle tracking solution, figure 8 shows how typical features such as sampling noise are avoided when using the present approach. We note in this context that the accuracy of the PDF at a given location under the hyperbolic formulation does not depend on how many points are used to discretise the solution, whereas under classical particle tracking

https://doi.org/10.1017/jfm.2025.11092 Published online by Cambridge University Press

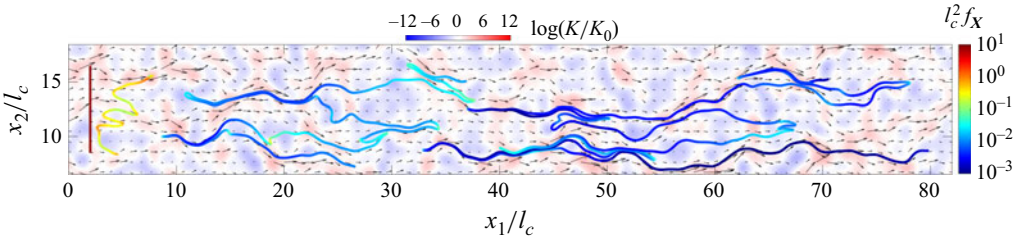


Figure 9. Evolution of the PDF of solute particle positions $f_{\boldsymbol{X}}$ in a heterogeneous medium for the initial condition (5.41*b*) and Péclet number $Pe = 10^3$, computed with (5.45*a*) along the locations of a material line at times $t/\tau_A = 0$, 2.7, 24.9 and 60.

Monte Carlo method, sampling leads to an error that is typically $\sim N^{-1/2}$. For the spatially targeted examples shown here, the computations with the present approach are faster by orders of magnitude. In this particular case, the hyperbolic formulation only requires integrating a total of two ODEs for the trajectory $\boldsymbol{x}(t;\boldsymbol{a})$ and the rest of the magnitudes are given by closed-form relations or quadratures: $\boldsymbol{\zeta}$ from (3.10), $\boldsymbol{B}$ from (3.16) and $\boldsymbol{A}$ from (D5). The solution is then directly computed using (5.44).

At time $t/\tau_A \approx 30$, a systematic error that we attribute to linearisation of the flow field can be observed in figure 8, especially for $Pe = 10^3$. As already noted, we do not employ relinearisation in this case. The final simulation times are small compared with the diffusion time ($t_{end}/\tau_D = 6 \times 10^{-2}$ for $Pe = 10^3$), but these errors illustrate that this is a global criterion and since the flow is heterogeneous, local variability of the flow field can lead to larger errors depending on the history of the velocity gradient tensor that each particular point of the plume samples over time.

Similarly, we compute from (5.45*a*) the evolution of the normalised concentration field along streamlines associated with the line injection (5.41*b*), i.e. at positions along an advected material line corresponding to this initial condition. These positions are given by $\boldsymbol{x}[t;\boldsymbol{x}_0(s^0)]$, where $\boldsymbol{x}_0(s^0) = (b_3,\ b_1 + (b_2 - b_1)s^0)^\top$, with $s^0 \in [0,1]$ the normalised position along the material line initially. At the initial time, we discretise the corresponding material line uniformly by taking values of s^0 given by $s_i^0 = (i-1)/(N_s - 1)$, $i = 1, \ldots, N_s$. The normalised position $s(t)$ along the line at later times is obtained as follows. First, join the positions $\boldsymbol{x}_i = \boldsymbol{x}[t;\boldsymbol{x}_0(s_i^0)]$ corresponding to adjacent $s_i(t)$ by straight segments of length $l_i(t) = |\boldsymbol{x}[t;\boldsymbol{x}_0(s_{i+1}^0)] - \boldsymbol{x}[t;\boldsymbol{x}_0(s_i^0)]|$. Then, the total length up to $\boldsymbol{x}_i$ is $L_i(t) = \sum_{j=1}^{i-1} l_i(t)$ and the corresponding normalised length at $\boldsymbol{x}_i$ is $s_i(t) = L_i(t)/L_{N_s}(t)$. The continuous version $s(t)$ can be constructed by interpolating along the straight line segments. If desired, it could be used to resample the line uniformly as it evolves in time.

To post-process the particle tracking simulations, we employ square bins of constant side h for a given time but adapt it for different times as the plume evolves and changes its characteristic spatial size. For the hyperbolic formulation, we subdivide the material line using $N_s = 5 \times 10^3$ points, whereas for the particle tracking simulations, we use $N = 10^6$ particles. Results at different times for $Pe = 10^3$ obtained using the hyperbolic formulation are shown in figure 9. A visual comparison with classical particle tracking results is shown in figure 10 for two different times and Péclet numbers $Pe = 10^3$ and 10^4. A more quantitative comparison with the results from (5.45*a*) with the reconstructed PDF interpolated at the locations of the material line can be found in figure 11, plotted along the normalised position along the material line, showing good agreement. Similar to the case of the point injection, a total of $2N_s$ ODEs are required to compute the trajectories that

https://doi.org/10.1017/jfm.2025.11092 Published online by Cambridge University Press

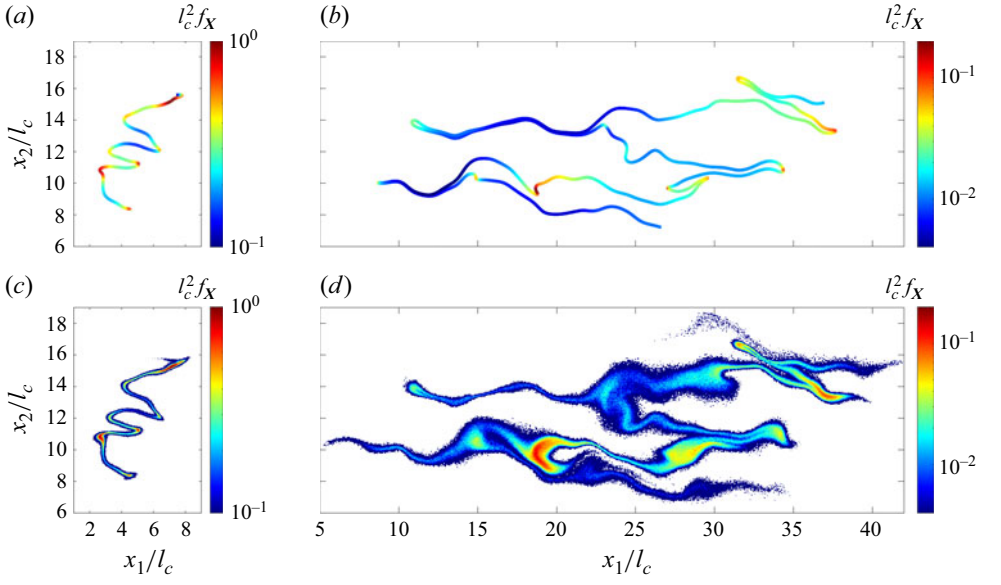


Figure 10. Evolution of the PDF of solute particle positions $f_{\boldsymbol{X}}$ in a heterogeneous medium for the initial condition (5.41*b*) and Péclet number $Pe = 10^3$, computed with (5.45*a*) for (*a*) $t = 2.7\tau_A$ and (*b*) $t = 24.9\tau_A$; and with Monte Carlo particle tracking simulations reconstructed with histograms for (*c*) $t = 2.7\tau_A$ with bin side $h = l_c/50$ and 309×394 bins, and (*d*) $t = 24.9\tau_A$ with $h = l_c/20$ and 750×245 bins.

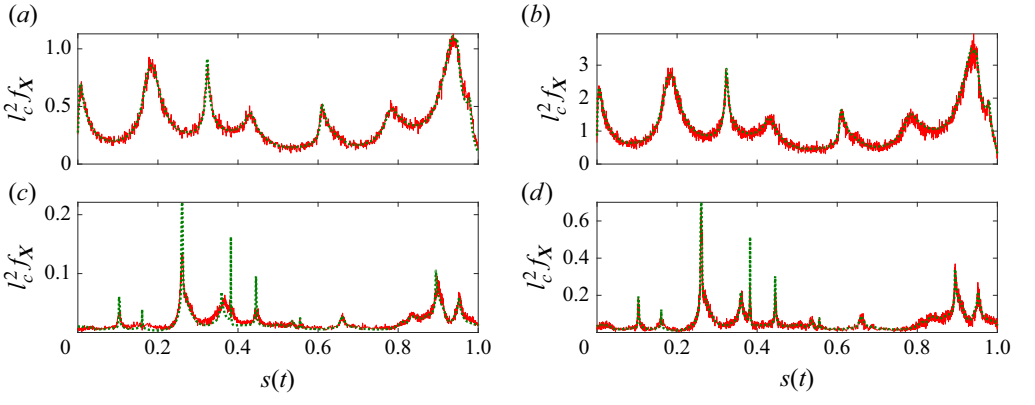


Figure 11. Evolution of the PDF of solute particle positions $f_{\boldsymbol{X}}$ in a heterogeneous medium for the initial condition (5.41*b*), computed with (5.45*a*) (dotted green line) and Monte Carlo particle tracking simulations (continuous red line) for (*a*) $t = 2.7\tau_A$ and $Pe = 10^3$, (*b*) $t = 24.9\tau_A$ and $Pe = 10^3$, (*c*) $t = 2.7\tau_A$ and $Pe = 10^4$, and (*d*) $t = 24.9\tau_A$ and $Pe = 10^4$. To reconstruct the PDFs from the particle tracking simulations, we use histograms with a bin side of (*a*) $h = l_c/50$, (*b*) $h = l_c/20$, (*c*) $h = l_c/100$ and (*d*) $h = l_c/50$; we then interpolate the PDF values at the locations of the advected material line from figure 10(*a*,*b*) with a zeroth-order interpolation scheme and plot it along $s(t)$ accordingly.

define the material line; then, $\boldsymbol{\zeta}$ is computed from (3.10), $\boldsymbol{B}$ from (3.16) and $\boldsymbol{A}$ from (D5); finally, the closed-form relation (5.45*a*) provides the normalised concentration profile. As discussed for figure 8, these results illustrate the benefits of the present formulation in avoiding sampling effects associated with reconstructing the concentration field from classical particle tracking, although we note again that we refrain from considering more involved reconstruction methods.

https://doi.org/10.1017/jfm.2025.11092 Published online by Cambridge University Press

6. Conclusions

We introduce a Lagrangian yet deterministic description of advective–diffusive transport based on a higher-dimensional Liouville master equation. The proposed approach is based on solving a closure problem for the first two moments of the particle distribution in a streamline coordinate system, ensuring that the marginalised moments of the Liouville description match those of the corresponding Fokker–Planck formulation. The validation of this formulation against particle tracking simulations at the Darcy scale under moderate heterogeneity reinforces its accuracy and potential for broader applications in subsurface flow and transport processes. As such, the framework presented here opens new avenues for the efficient and accurate simulation of mixing phenomena in complex, heterogeneous flow systems, with implications for both environmental and industrial applications where detailed, high-fidelity solute transport predictions are critical.

By formulating a noise term with time-independent random coefficients, we circumvent the need for stochastic calculus, providing a deterministic Lagrangian framework for solute particle statistics that is both computationally efficient and free from the limitations of traditional Monte Carlo based particle tracking algorithms and grid-based PDE solvers. The approach is demonstrated to be effective in tracing solute plumes of arbitrary shape, including singular profiles with infinite gradients, as well as applicable for arbitrary Péclet numbers. It retains diffusion in all directions and is therefore applicable to compute late-time dynamics for which lamella-based formulations tend to break down. This formulation significantly reduces computational cost by eliminating the need for grid-based methods or direct sampling of particle trajectories. In particular, it has the major advantage of allowing concentration fields to be easily computed at arbitrary spatial positions. Among other things, this makes it possible to target low-concentration regions, associated with improbable trajectories, directly. The present framework extends previous works based on linearising the drift term (Meunier & Villermaux 2010; Dentz *et al.* 2018) and introduces a relinearisation procedure that allows us to account for nonlinearities in the flow.

We have focused on bidimensional incompressible steady flows and constant diffusion coefficient, but compressible flows can be treated using the present framework; they simply lead to a transformation Jacobian along characteristic lines in the augmented phase space that has a non-unitary determinant, which means that the joint PDF is not constant along characteristics. We expect the extension to three dimensions to be relatively simple using the so-called Protean frame (Lester *et al.* 2018). Extensions to unsteady flows and spatially variable, non-isotropic dispersion also appear to pose no major barriers and will be presented elsewhere, along with the treatment of boundary conditions such as at impermeable surfaces. The formulation presented here is, nevertheless, not exempt from limitations. At present, it can only be used to study one-point space–time statistics (i.e. the concentration field) of a transported scalar, as opposed to classical particle tracking methods, which capture multi-point statistics along particle trajectories. Extensions to reactive transport would also be desirable but pose significant challenges, especially for nonlinear interactions. Other extension possibilities for the present framework include accounting for incomplete knowledge of the flow velocities or the concentration field itself (Dagan 1984; Balkovsky & Fouxon 1999; Dentz & de Barros 2015). Finally, we point out that this formulation may be used to study reverse-time diffusion processes (Anderson 1982), thanks to the hyperbolicity of the Liouville master equation.

Funding. The authors acknowledge funding by the European Union (ERC Uplift 101115760). TA further acknowledges financial support through the HydroPoreII project (PID2022-137652NB-C42), funded by MICIU/AEI/10.13039/501100011033 and by ERDF/EU. Views and opinions expressed are, however, those of

https://doi.org/10.1017/jfm.2025.11092 Published online by Cambridge University Press

the authors only, and do not necessarily reflect those of the European Union or the European Research Council Executive Agency. Neither the European Union nor the granting authority can be held responsible for them.

Declaration of interests. The authors report no conflict of interest.

Data availability statement. The data that support the findings of this study are available upon request.

Appendix A. Derivation of the Liouville master equation

Let $\Delta(\boldsymbol{\alpha}, \boldsymbol{\beta}; \boldsymbol{x}, \boldsymbol{\xi}) = \delta(\boldsymbol{x} - \boldsymbol{\alpha})\delta(\boldsymbol{\xi} - \boldsymbol{\beta})$ and consider $\varPi(\boldsymbol{X}, \boldsymbol{\Xi}; \boldsymbol{x}, \boldsymbol{\xi}, t) = \Delta(\boldsymbol{X}(t), \boldsymbol{\Xi}; \boldsymbol{x}, \boldsymbol{\xi})$. This is sometimes called a raw (joint) PDF (Tartakovsky & Gremaud 2015), because, taking averages over the random variables $\boldsymbol{X}(t)$ and $\boldsymbol{\Xi}$,

$$\overline{\varPi(\boldsymbol{X}, \boldsymbol{\Xi}; \boldsymbol{x}, \boldsymbol{\xi}, t)} = \int_{\mathbb{R}^d} \mathrm{d}\boldsymbol{x}' \int_{\mathbb{R}^d} \mathrm{d}\boldsymbol{\xi}'\, \Delta(\boldsymbol{x}', \boldsymbol{\xi}'; \boldsymbol{x}, \boldsymbol{\xi}) f_{\boldsymbol{X}\boldsymbol{\Xi}}(\boldsymbol{x}', \boldsymbol{\xi}'; t) = f_{\boldsymbol{X}\boldsymbol{\Xi}}(\boldsymbol{x}, \boldsymbol{\xi}; t). \quad \text{(A1)}$$

Differentiating $\varPi(\boldsymbol{X}, \boldsymbol{\Xi}; \boldsymbol{x}, \boldsymbol{\xi}, t)$ with respect to t and applying the chain rule one has

$$\frac{\partial \varPi}{\partial t} = \frac{\mathrm{d}\boldsymbol{X}}{\mathrm{d}t} \cdot \nabla_{\boldsymbol{\alpha}} \Delta = -\frac{\mathrm{d}\boldsymbol{X}}{\mathrm{d}t} \cdot \nabla \Delta = -\frac{\mathrm{d}\boldsymbol{X}}{\mathrm{d}t} \cdot \nabla \varPi, \quad \text{(A2)}$$

where as usual ∇ with no subscript differentiates with respect to the spatial position $\boldsymbol{x}$, i.e. the third argument of both Δ and $\varPi$. Thus,

$$\frac{\partial \varPi}{\partial t} + \nabla \cdot \frac{\mathrm{d}\boldsymbol{X}}{\mathrm{d}t} \varPi = 0, \quad \text{(A3)}$$

and using (2.5*a*),

$$\frac{\partial \varPi}{\partial t} + \nabla \cdot [\boldsymbol{u}(\boldsymbol{X}, t) + \boldsymbol{s}(\boldsymbol{X}, \boldsymbol{\Xi}, t)]\, \varPi = 0. \quad \text{(A4)}$$

Ensemble averaging (A4) leads directly to the Liouville equation (2.6*a*).

Appendix B. Moment equations

To compute moments within the method of characteristics formulation presented in § 2.2, consider an arbitrary function $\boldsymbol{g}(t; \boldsymbol{\Xi}, \boldsymbol{X}_0)$. Its ensemble average is given by (Halmos 1950)

$$\overline{\boldsymbol{g}}(t) = \overline{\boldsymbol{g}(t; \boldsymbol{\Xi}, \boldsymbol{X}_0)} = \int_{\mathbb{R}^d} \mathrm{d}\boldsymbol{x}_0 \int_{\mathbb{R}^d} \mathrm{d}\boldsymbol{\xi}\, \boldsymbol{g}(t; \boldsymbol{\xi}, \boldsymbol{x}_0) f_{\boldsymbol{X}}^0(\boldsymbol{x}_0) f_{\boldsymbol{\Xi}}(\boldsymbol{\xi}), \quad \text{(B1)}$$

often termed the law of the unconscious statistician. We can compute the associated fluctuations as

$$\boldsymbol{g}'(t; \boldsymbol{\Xi}, \boldsymbol{X}_0) = \boldsymbol{g}(t; \boldsymbol{\Xi}, \boldsymbol{X}_0) - \overline{\boldsymbol{g}}(t), \quad \text{(B2)}$$

from which any central moment of interest follows. For example, the covariance matrix is

$$\overline{g_i' g_j'}(t) = \int_{\mathbb{R}^d} \mathrm{d}\boldsymbol{x}_0 \int_{\mathbb{R}^d} \mathrm{d}\boldsymbol{\xi}\, \left[g_i(t; \boldsymbol{\xi}, \boldsymbol{x}_0) - \overline{g}_i(t)\right] \left[g_j(t; \boldsymbol{\xi}, \boldsymbol{x}_0) - \overline{g}_j(t)\right] f_{\boldsymbol{X}}^0(\boldsymbol{x}_0) f_{\boldsymbol{\Xi}}(\boldsymbol{\xi}). \quad \text{(B3)}$$

To derive a set of central moment equations using the random differential equation description of the Liouville characteristics, (2.5), we start by decomposing the stochastic variables into averages and fluctuations, $(\cdot) = \overline{(\cdot)} + (\cdot)'$.

https://doi.org/10.1017/jfm.2025.11092 Published online by Cambridge University Press

This leads to the following set of equations for the components of the average $\overline{\boldsymbol{X}}(t)$ and covariance matrix $\boldsymbol{\kappa}(t)$:

$$\frac{\mathrm{d}\overline{X}_i(t)}{\mathrm{d}t} = \overline{u}_i(t) + \overline{s}_i(t), \tag{B4a}$$

$$\frac{\mathrm{d}\kappa_{ij}(t)}{\mathrm{d}t} = \overline{u_i' X_j'}(t) + \overline{u_j' X_i'}(t) + \overline{s_i' X_j'}(t) + \overline{s_j' X_i'}(t). \tag{B4b}$$

In the remainder of this appendix, we employ Einstein sum notation, meaning repeated indices are summed over.

The unclosed terms of (B4*a*) can be approximated using Taylor expansion. For the velocity term, we find that

$$u_i(t) \approx u_i(\overline{\boldsymbol{X}}(t), t) + X_l' \left.\frac{\partial u_i}{\partial x_l}\right|_{\overline{\boldsymbol{X}}(t),t} + \frac{1}{2} X_l' X_m' \left.\frac{\partial^2 u_i}{\partial x_l \partial x_m}\right|_{\overline{\boldsymbol{X}}(t),t}, \tag{B5}$$

truncating terms of the order of fluctuations to the third power or higher. Similarly, for the source term, one has

$$\begin{aligned} s_i(t) \approx & s_i(\overline{\boldsymbol{X}}(t), \overline{\boldsymbol{\Xi}}, t) + X_l' \left.\frac{\partial s_i}{\partial x_l}\right|_{\overline{\boldsymbol{X}}(t),\overline{\boldsymbol{\Xi}},t} + \Xi_l' \left.\frac{\partial s_i}{\partial \xi_l}\right|_{\overline{\boldsymbol{X}}(t),\overline{\boldsymbol{\Xi}},t} + \frac{1}{2}\theta_{lm} \left.\frac{\partial^2 s_i}{\partial \xi_l \partial \xi_m}\right|_{\overline{\boldsymbol{X}}(t),\overline{\boldsymbol{\Xi}},t} \\ & + \frac{1}{2}\zeta_{lm}(t) \left.\frac{\partial^2 s_i}{\partial \xi_l \partial x_m}\right|_{\overline{\boldsymbol{X}}(t),\overline{\boldsymbol{\Xi}},t} + \frac{1}{2}\kappa_{lm}(t) \left.\frac{\partial^2 s_i}{\partial x_l \partial x_m}\right|_{\overline{\boldsymbol{X}}(t),\overline{\boldsymbol{\Xi}},t}. \end{aligned} \tag{B6}$$

In (B4*a*) for the mean position, the flow field and source term contributions proportional to first-order moments and derivatives disappear under averaging, and higher-order terms may be neglected to leading order, yielding

$$\frac{\mathrm{d}\overline{\boldsymbol{X}}(t)}{\mathrm{d}t} = \boldsymbol{u}(\overline{\boldsymbol{X}}(t), t) + \boldsymbol{s}(\overline{\boldsymbol{X}}(t), \overline{\boldsymbol{\Xi}}, t). \tag{B7}$$

The terms involving first derivatives are, however, needed in the second moment (B4*b*) and (B11), where they give rise to leading-order contributions. We thus have a closure problem involving (i) the covariances $\kappa_{ij}(t)$ of positions themselves, (ii) the covariances $\zeta_{ij}(t) = \overline{\Xi_i' X_j'}(t)$ of the random coefficients and positions, (iii) the average coefficients $\overline{\boldsymbol{\Xi}}$, and (iv) the covariances $\theta_{ij} = \overline{\Xi_i' \Xi_j'}$ of the random coefficients. Items (iii) and (iv) can be imposed arbitrarily, and we compute the remaining quantities below.

We proceed for (i) by expanding each of the terms in (B4*b*) as before. We find that

$$\begin{aligned} \overline{u_i' X_j'}(t) = \overline{(u_i(t) - \overline{u}_i(t))\, X_j'(t)} &\approx \overline{\left(u_i(\overline{\boldsymbol{X}}(t), t) + X_l' \left.\frac{\partial u_i}{\partial x_l}\right|_{\overline{\boldsymbol{X}}(t),t} - \overline{u}_i(t)\right) X_j'} \\ &= \kappa_{lj}(t) \left.\frac{\partial u_i}{\partial x_l}\right|_{\overline{\boldsymbol{X}}(t),t} \end{aligned} \tag{B8}$$

and

$$\overline{s_i' X_j'}(t) \approx \zeta_{lj}(t) \left.\frac{\partial s_i}{\partial \xi_l}\right|_{\overline{\boldsymbol{X}}(t),\overline{\boldsymbol{\Xi}},t} + \kappa_{lj}(t) \left.\frac{\partial s_i}{\partial x_l}\right|_{\overline{\boldsymbol{X}}(t),\overline{\boldsymbol{\Xi}},t}, \tag{B9}$$

https://doi.org/10.1017/jfm.2025.11092 Published online by Cambridge University Press

so that

$$\frac{\mathrm{d}\boldsymbol{\kappa}}{\mathrm{d}t} = [\boldsymbol{\epsilon} + \boldsymbol{\eta}]\boldsymbol{\kappa} + \boldsymbol{\kappa}[\boldsymbol{\epsilon} + \boldsymbol{\eta}]^\top + \boldsymbol{\varphi}\boldsymbol{\zeta} + [\boldsymbol{\varphi}\boldsymbol{\zeta}]^\top, \tag{B10}$$

where $\boldsymbol{\epsilon}(t) = (\boldsymbol{\nabla}\boldsymbol{u})|^\top_{\overline{\boldsymbol{X}}(t),t}$, $\boldsymbol{\eta}(t) = (\boldsymbol{\nabla}s)|^\top_{\overline{\boldsymbol{X}}(t),\overline{\boldsymbol{\Xi}},t}$ and $\boldsymbol{\varphi}(t) = (\boldsymbol{\nabla}_{\boldsymbol{\xi}}s)|^\top_{\overline{\boldsymbol{X}}(t),\overline{\boldsymbol{\Xi}},t}$.

Differentiating according to the definition, the covariances (ii) obey

$$\frac{\mathrm{d}\zeta_{ij}(t)}{\mathrm{d}t} = \overline{\Xi_i' u_j'}(t) + \overline{\Xi_i' s_j'}(t), \tag{B11}$$

where the unclosed terms may, as before, be approximated by

$$\overline{\Xi_i' u_j'}(t) \approx \zeta_{il}(t)\ \left.\frac{\partial u_j}{\partial x_l}\right|_{\overline{\boldsymbol{X}}(t),t} \tag{B12}$$

and

$$\overline{\Xi_i' s_j'}(t) \approx \theta_{il}\ \left.\frac{\partial s_j}{\partial \xi_l}\right|_{\overline{\boldsymbol{X}}(t),\overline{\boldsymbol{\Xi}},t} + \zeta_{il}(t)\ \left.\frac{\partial s_j}{\partial x_l}\right|_{\overline{\boldsymbol{X}}(t),\overline{\boldsymbol{\Xi}},t}. \tag{B13}$$

Thus,

$$\frac{\mathrm{d}\boldsymbol{\zeta}}{\mathrm{d}t} = \boldsymbol{\zeta}[\boldsymbol{\epsilon} + \boldsymbol{\eta}]^\top + \boldsymbol{\theta}\boldsymbol{\varphi}^\top. \tag{B14}$$

In summary, assume that the flow field $\boldsymbol{u}$ and source term $\boldsymbol{s}$ are known and twice smoothly differentiable, and that the first two moments of the random noise coefficients $\boldsymbol{\Xi}$ are also known and finite. Then, a closed system for the first two moments of positions $\boldsymbol{X}(t)$ governed by the random differential (2.5) is given by (B7), (B10) and (B14), which are to be solved with initial conditions that may in general be related to the corresponding PDFs by ensemble averaging:

$$\overline{X}_i(0) = \overline{X}_i^0 = \int_{\mathbb{R}^d} \mathrm{d}\boldsymbol{x} \int_{\mathbb{R}^d} \mathrm{d}\boldsymbol{\xi}\ x_i\, f_{\boldsymbol{X}}^0(\boldsymbol{x})\, f_{\boldsymbol{\Xi}}(\boldsymbol{\xi}), \tag{B15a}$$

$$\kappa_{ij}(0) = \kappa_{ij}^0 = \int_{\mathbb{R}^d} \mathrm{d}\boldsymbol{x} \int_{\mathbb{R}^d} \mathrm{d}\boldsymbol{\xi}\ \big(x_i - \overline{X}_i^0\big)\big(x_j - \overline{X}_j^0\big)\, f_{\boldsymbol{X}}^0(\boldsymbol{x})\, f_{\boldsymbol{\Xi}}(\boldsymbol{\xi}), \tag{B15b}$$

$$\zeta_{ij}(0) = \int_{\mathbb{R}^d} \mathrm{d}\boldsymbol{x} \int_{\mathbb{R}^d} \mathrm{d}\boldsymbol{\xi}\ (\xi_i - \overline{\Xi}_i)\big(x_j - \overline{X}_j^0\big)\, f_{\boldsymbol{X}}^0(\boldsymbol{x})\, f_{\boldsymbol{\Xi}}(\boldsymbol{\xi}) = 0. \tag{B15c}$$

Similarly, the moments of the coefficients are

$$\overline{\Xi}_i = \int_{\mathbb{R}^d} \mathrm{d}\boldsymbol{\xi}\ \xi_i\, f_{\boldsymbol{\Xi}}(\boldsymbol{\xi}), \qquad \theta_{ij} = \int_{\mathbb{R}^d} \mathrm{d}\boldsymbol{\xi}\ (\xi_i - \overline{\Xi}_i)(\xi_j - \overline{\Xi}_j)\, f_{\boldsymbol{\Xi}}(\boldsymbol{\xi}). \tag{B16}$$

Note that the distribution of initial positions is arbitrary, so that in particular this description holds separately for any given deterministic (i.e. point) initial condition.

Appendix C. Analytical hyperbolic description of elementary stochastic processes

Here we illustrate the Liouville approach by showing explicitly how it can be used to reproduce the PDF of simple one-dimensional stochastic processes, namely the Wiener process (Brownian motion) with constant drift and the Ornstein–Uhlenbeck process. Using the theoretical framework derived in § 2 with a single random coefficient Ξ, we find constraints for the deterministic dependency $\varphi(t)$ of the noise term with time, based on

https://doi.org/10.1017/jfm.2025.11092 Published online by Cambridge University Press

the moment equations. In addition, full equivalency of the PDFs requires the random coefficient to be a standard normal random variable, $\Xi \sim \mathcal{N}(0, 1)$. These solutions were introduced in Domínguez-Vázquez *et al.* (2024*b*); we discuss them here for completeness.

C.1 *Brownian motion with constant drift*

Consider the one-dimensional Langevin equation

$$\mathrm{d}X(t) = v\mathrm{d}t + \sqrt{2D}\mathrm{d}W_t, \qquad X(0) = x_0, \tag{C1}$$

where the diffusion coefficient D, the drift term v and the (deterministic) initial particle location x_0 are constant, and W_t is a Wiener process. We seek a hyperbolic description of a process $X(t)$ with the same point statistics, i.e. such that the FPE for the PDF $f_X(x; t)$ is given by

$$\frac{\partial f_X}{\partial t} + v\frac{\partial f_X}{\partial x} = D\frac{\partial^2 f_X}{\partial x^2}, \qquad f_X(x; 0) = \delta(x - x_0), \tag{C2}$$

with the well-known solution (Risken 1996)

$$f_X(x; t) = \frac{1}{\sqrt{4\pi Dt}} \exp\left(-\frac{(x - vt - x_0)^2}{4Dt}\right). \tag{C3}$$

The first two central moments of $f_X(x; t)$ are described by the equations

$$\frac{\mathrm{d}\overline{X}(t)}{\mathrm{d}t} = v, \qquad \frac{\mathrm{d}\sigma_X^2(t)}{\mathrm{d}t} = 2D, \tag{C4a}$$

$$\overline{X}(0) = x_0, \qquad \sigma_X^2(0) = 0, \tag{C4b}$$

with the solution

$$\overline{X}(t) = x_0 + vt, \qquad \sigma_X^2(t) = 2Dt, \tag{C5}$$

where $\sigma_X^2 = \kappa = \overline{X'^2}$.

Proceeding with the Liouville approach, we search for a stochastic source term based on a single random coefficient such that the same first two moments coincide with (C5). We thus start with the random differential equation

$$\frac{\mathrm{d}X(t)}{\mathrm{d}t} = v + \Xi\varphi(t), \qquad X(0) = x_0, \tag{C6}$$

whose governing PDF equation is the Liouville equation

$$\frac{\partial f_{X\Xi}}{\partial t} + [v + \xi\varphi(t)]\frac{\partial f_{X\Xi}}{\partial x} = 0, \qquad f_{X\Xi}(x, \xi; 0) = \delta(x - x_0) f_\Xi(\xi). \tag{C7}$$

Then, the source term $\varphi(t)$ can be found by looking at the moment equations

$$\frac{\mathrm{d}\overline{X}(t)}{\mathrm{d}t} = v + \overline{\Xi}\varphi(t), \qquad \frac{\mathrm{d}\sigma_X^2(t)}{\mathrm{d}t} = 2\zeta(t)\varphi(t), \qquad \frac{\mathrm{d}\zeta(t)}{\mathrm{d}t} = \sigma_\Xi^2\varphi(t), \tag{C8}$$

with $\sigma_\Xi^2 = \theta = \overline{\Xi'^2}$ and $\zeta = \overline{\Xi' X'}$. Comparing with (C4*a*), these provide the following conditions to be fulfilled in order for the PDF of X in the Liouville description to solve the

https://doi.org/10.1017/jfm.2025.11092 Published online by Cambridge University Press

FPE (C2):

$$\overline{\Xi}\varphi(t) = 0, \qquad \zeta(t)\varphi(t) = D, \tag{C9a}$$

$$\frac{\mathrm{d}\zeta(t)}{\mathrm{d}t} = \sigma_\Xi^2 \varphi(t), \qquad \zeta(0) = 0. \tag{C9b}$$

We conclude that the average coefficient must be zero, $\overline{\Xi} = 0$. The standard deviation is arbitrary because it can be absorbed into $\varphi(t)$. We choose unity for simplicity, $\sigma_\Xi^2 = 1$. With this choice, $\zeta(t) = \sigma_X(t) = \sqrt{2Dt}$, and the deterministic time dependence of the source term is

$$\varphi(t) = \frac{D}{\sigma_X(t)} = \sqrt{\frac{D}{2t}}. \tag{C10}$$

Note that so far we have not imposed the full PDF $f_\Xi(\xi)$ of the random coefficient, but only its first two moments.

Now, we look at the characteristic lines of the Liouville master equation,

$$\frac{\mathrm{d}\hat{x}(t)}{\mathrm{d}t} = v + \xi\varphi(t), \qquad \frac{\mathrm{d}\hat{f}_{X\Xi}(t)}{\mathrm{d}t} = 0, \tag{C11a}$$

$$\hat{x}(0) = X_0, \qquad \hat{f}_{X\Xi}(0) = \delta(X_0 - x_0) f_\Xi(\xi), \tag{C11b}$$

where $X_0 = x_0$ with unit probability, i.e. its PDF $f_{X_0} = \delta(X_0 - x_0)$. The solution is

$$\hat{x}(t) = x_0 + vt + \xi\sqrt{2Dt}, \tag{C12a}$$

$$\hat{f}_{X\Xi}(t) = \delta[\hat{x}_0(\xi, x, t) - x_0] f_\Xi(\xi). \tag{C12b}$$

Inverting $\hat{x}(t)$ for x_0 we obtain

$$f_{X\Xi}(x, \xi; t) = \delta(x - vt - \xi\sqrt{2Dt} - x_0) f_\Xi(\xi). \tag{C13}$$

Note that, as the source term is independent of the spatial coordinate and the flow is incompressible, the determinant of the transformation Jacobian is unity, $J(t) = 1$; see (2.9). Marginalisation along ξ with the aid of the properties of the Dirac delta leads to

$$f_X(x; t) = \int_{\mathbb{R}} \mathrm{d}\xi\, \delta(x - vt - \xi\sqrt{2Dt} - x_0) f_\Xi(\xi) = \frac{1}{\sigma_X(t)} f_\Xi\left(\frac{x - \overline{X}(t)}{\sigma_X(t)}\right). \tag{C14}$$

This is a generalisation of (C3) for systems that may have non-Gaussian noise. If the random coefficient follows a standard normal distribution, $\Xi \sim \mathcal{N}(0, 1)$, these results for the point statistics coincide. For different distributions of the random coefficient, other solutions may be found that do not correspond to the Fokker–Planck equation (C2) nor the Langevin equation (C1) but may describe the same statistics up to the second moment if $\overline{\Xi} = 0$ and $\sigma_\Xi^2 = 1$. For completeness, we note that, for an arbitrary initial PDF $f_{X_0}(x_0)$, the solution (C14) becomes

$$f_X(x; t) = \int_{\mathbb{R}} \mathrm{d}\xi f_{X_0}(x - vt - \xi\sqrt{2Dt}) f_\Xi(\xi). \tag{C15}$$

Relations (C14) and (C15) are respectively depicted in figures 1(*a*) and (*b*) schematically.

https://doi.org/10.1017/jfm.2025.11092 Published online by Cambridge University Press

C.2 *Ornstein–Uhlenbeck process*

The Langevin equation for the Ornstein–Uhlenbeck process is

$$\mathrm{dX}(t) = -\alpha \mathrm{X}(t)\mathrm{d}t + \sqrt{2D}\mathrm{d}W_t, \qquad \mathrm{X}(0) = x_0, \tag{C16}$$

where the drift term is linear in position with proportionality constant α and the diffusion coefficient D is constant. As before, we take the initial position $X_0 = X(0)$ to be deterministically equal to x_0 for simplicity. We seek a hyperbolic description of a process $X(t)$ that solves the same FPE,

$$\frac{\partial f_X}{\partial t} - \alpha \frac{\partial}{\partial x}(x f_X) = D \frac{\partial^2 f_X}{\partial x^2}, \qquad f_X(x;0) = \delta(x - x_0), \tag{C17}$$

whose solution is well known (Risken 1996):

$$f_X(x;t) = \left(\frac{\alpha}{2\pi D\left(1 - \mathrm{e}^{-2\alpha t}\right)}\right)^{1/2} \exp\left(-\frac{\alpha\left(x - \mathrm{e}^{-\alpha t}\right)^2}{2\pi D\left(1 - \mathrm{e}^{-2\alpha t}\right)}\right). \tag{C18}$$

The corresponding moment equations are

$$\frac{\mathrm{d}\overline{X}(t)}{\mathrm{d}t} = -\alpha \overline{X}(t), \qquad \frac{\mathrm{d}\sigma_X^2(t)}{\mathrm{d}t} = -2\alpha\sigma_X^2(t) + 2D, \tag{C19a}$$

$$\overline{X}(0) = x_0, \qquad \sigma_X^2(0) = 0, \tag{C19b}$$

with the solution

$$\overline{X}(t) = x_0 \mathrm{e}^{-\alpha t}, \qquad \sigma_X^2(t) = \frac{D}{\alpha}\left(1 - \mathrm{e}^{-2\alpha t}\right). \tag{C20}$$

Proceeding with the Liouville approach as before, we define the following stochastic equation with a random coefficient:

$$\frac{\mathrm{d}X}{\mathrm{d}t} = -\alpha X + \Xi\varphi, \qquad X(0) = x_0. \tag{C21}$$

Here the joint PDF is governed by the Liouville equation

$$\frac{\partial f_{X\Xi}}{\partial t} + \frac{\partial}{\partial x}\left[(-\alpha x + \xi\varphi)\, f_{X\Xi}\right] = 0, \qquad f_{X\Xi}(x,\xi;0) = \delta(x - x_0) f_\Xi(\xi). \tag{C22}$$

The corresponding moment equations are

$$\frac{\mathrm{d}\overline{X}(t)}{\mathrm{d}t} = -\alpha \overline{X}(t) + \overline{\Xi}\varphi(t), \qquad \frac{\mathrm{d}\sigma_X^2(t)}{\mathrm{d}t} = -2\alpha\sigma_X^2(t) + 2\zeta(t)\varphi(t), \tag{C23}$$

$$\frac{\mathrm{d}\zeta(t)}{\mathrm{d}t} = -\alpha\zeta(t) + \sigma_\Xi^2\varphi(t). \tag{C24}$$

When compared with (C19*a*), these result in the following conditions for the source term:

$$\overline{\Xi}\varphi(t) = 0, \qquad \zeta(t)\varphi(t) = D, \tag{C25a}$$

$$\frac{\mathrm{d}\zeta(t)}{\mathrm{d}t} = -\alpha\zeta(t) + \sigma_\Xi^2\varphi(t), \qquad \zeta(0) = 0. \tag{C25b}$$

As in § C.1, we obtain $\overline{\Xi} = 0$, arbitrarily set $\sigma_\Xi^2 = 1$, and find that $\zeta(t) = \sigma_X(t)$, such that

$$\varphi(t) = \frac{D}{\sigma_X(t)} = \sqrt{\frac{\alpha D}{1 - \mathrm{e}^{-2\alpha t}}}. \tag{C26}$$

https://doi.org/10.1017/jfm.2025.11092 Published online by Cambridge University Press

Then, we look at the characteristic lines of the master equation (C22),

$$\frac{\mathrm{d}\hat{x}(t)}{\mathrm{d}t} = -\alpha\hat{x}(t) + \xi\varphi(t), \qquad \frac{\mathrm{d}\hat{f}_{X\Xi}(t)}{\mathrm{d}t} = \alpha\hat{f}_{X\Xi}(t), \tag{C27a}$$

$$\hat{x}(0) = X_0, \qquad \hat{f}_{X\Xi}(0) = \delta(X_0 - x_0) f_\Xi(\xi), \tag{C27b}$$

whose solution is given by

$$\hat{x}(t) = x_0 \mathrm{e}^{-\alpha t} + \xi\sqrt{\frac{D}{\alpha}\left(1 - \mathrm{e}^{-2\alpha t}\right)}, \tag{C28a}$$

$$\hat{f}_{X\Xi}(t) = \mathrm{e}^{\alpha t}\delta[\hat{x}_0(\xi, x, t) - x_0] f_\Xi(\xi). \tag{C28b}$$

Note that the determinant of the transformation Jacobian in (2.9) is in this case $J(t) = \mathrm{e}^{-\alpha t}$, which differs from unity because the flow field is not incompressible. Inverting the characteristics $\hat{x}(t)$ for the initial position and changing variables in the Dirac delta leads to

$$f_{X\Xi}(x, \xi; t) = \delta\left(x - \xi\sqrt{\frac{D}{\alpha}(1 - \mathrm{e}^{-2\alpha t})} - \mathrm{e}^{-\alpha t} x_0\right) f_\Xi(\xi). \tag{C29}$$

Marginalisation along ξ yields

$$f_X(x; t) = \frac{1}{\sigma_X(t)} f_\Xi\left(\frac{x - \overline{X}(t)}{\sigma_X(t)}\right), \tag{C30}$$

given in terms of the moments (C20). As with the description of Brownian motion, if the random coefficient follows a standard normal distribution, (C30) reduces to (C18), whereas different distributions lead to generalised processes with a different PDF. For an arbitrary initial condition, one has

$$f_X(x; t) = \int_{\mathbb{R}} \mathrm{d}\xi \mathrm{e}^{\alpha t} f_{X_0}\left(\mathrm{e}^{\alpha t}\left[x - \xi\sqrt{\frac{D}{\alpha}(1 - \mathrm{e}^{-2\alpha t})}\right] - x_0\right) f_\Xi(\xi). \tag{C31}$$

Appendix D. Lagrangian relations in the streamline coordinate frame

Here we discuss infinitesimal deformation and diffusion in the streamline coordinate frame following Dentz *et al.* (2016, 2018). The movement of a fluid element starting at a given initial position $\boldsymbol{x}_0$ at the initial time t_0 is given by

$$\frac{\mathrm{d}\boldsymbol{x}(t; \boldsymbol{x}_0, t_0)}{\mathrm{d}t} = \boldsymbol{v}(t; \boldsymbol{x}_0, t_0), \qquad \boldsymbol{x}(t_0; \boldsymbol{x}_0, t_0) = \boldsymbol{x}_0, \tag{D1}$$

where $\boldsymbol{v}(t; \boldsymbol{x}_0, t_0) = \boldsymbol{u}[\boldsymbol{x}(t; \boldsymbol{x}_0, t_0)]$ is the Lagrangian velocity along the path of the fluid element, which corresponds to a streamline because the Eulerian flow field $\boldsymbol{u}$ has been assumed independent of time. As before, we sometimes omit some or all the arguments beyond the first. Comparing to (3.2*a*) with $\overline{\boldsymbol{\Xi}} = \boldsymbol{0}$, we see that under local linearisation (D1) equals the mean path of a blob whose initial average position is $\boldsymbol{x}_0$, i.e. $\boldsymbol{x}(t; \overline{\boldsymbol{X}}^0) = \overline{\boldsymbol{X}}(t)$. This motivates us to analyse the evolution of a material fluid element whose length and orientation are defined by the difference between two nearby fluid particles, following previous work by Dentz *et al.* (2016) for fluid-induced deformation,

$$\boldsymbol{z}(t; \boldsymbol{x}_0 + \delta\boldsymbol{x}_0, \boldsymbol{x}_0) = \boldsymbol{x}(t; \boldsymbol{x}_0 + \delta\boldsymbol{x}_0) - \boldsymbol{x}(t; \boldsymbol{x}_0), \tag{D2}$$

https://doi.org/10.1017/jfm.2025.11092 Published online by Cambridge University Press

since the last term on the right-hand side simply represents the mean plume movement $\overline{\boldsymbol{X}}(t)$ and can thus be easily restored. Linearising the flow, i.e. Taylor expanding the time derivative of (D2) according to (D1) for small deformations, we have

$$\frac{\mathrm{d}\boldsymbol{z}(t;\boldsymbol{x}_0+\delta\boldsymbol{x}_0,\boldsymbol{x}_0)}{\mathrm{d}t}=\boldsymbol{\epsilon}(t;\boldsymbol{x}_0)\boldsymbol{z}(t;\boldsymbol{x}_0+\delta\boldsymbol{x}_0,\boldsymbol{x}_0), \tag{D3}$$

with $\boldsymbol{\epsilon}(t;\boldsymbol{x}_0)$ the velocity gradient tensor along the trajectory $\boldsymbol{x}(t;\boldsymbol{x}_0)$. We now change coordinates to the streamline system. Positions $\boldsymbol{x}'$ in this moving coordinate system are related to positions $\boldsymbol{x}$ in the fixed one via a rotation according to the velocity vector orientation at the mean plume position,

$$\boldsymbol{x}'=\boldsymbol{A}^{\top}(t;\boldsymbol{x}_0)[\boldsymbol{x}-\boldsymbol{x}(t;\mathbf{x}_0)], \tag{D4}$$

with

$$\boldsymbol{A}(t;\boldsymbol{x}_0)=\frac{1}{v(t;\boldsymbol{x}_0)}\begin{bmatrix}v_1(t;\boldsymbol{x}_0) & -v_2(t;\boldsymbol{x}_0)\\ v_2(t;\boldsymbol{x}_0) & v_1(t;\boldsymbol{x}_0)\end{bmatrix}, \tag{D5}$$

where $v(t;\boldsymbol{x}_0)=|\boldsymbol{v}(t;\boldsymbol{x}_0)|$. Equation (D3) in this coordinate system reads as

$$\frac{\mathrm{d}z'(t;\boldsymbol{x}_0+\delta\boldsymbol{x}_0,\boldsymbol{x}_0)}{\mathrm{d}t}=\boldsymbol{\epsilon}'(t;\boldsymbol{x}_0)z'(t;\boldsymbol{x}_0+\delta\boldsymbol{x}_0,\boldsymbol{x}_0), \tag{D6}$$

with the velocity gradient tensor in this frame given by

$$\boldsymbol{\epsilon}'(t;\boldsymbol{x}_0)=\begin{bmatrix}\alpha'(t;\boldsymbol{x}_0) & \gamma'(t;\boldsymbol{x}_0)\\ 0 & -\alpha'(t;\boldsymbol{x}_0)\end{bmatrix}, \tag{D7}$$

whose components are computed as

$$\alpha'(t;\boldsymbol{x}_0)=\frac{1}{v(t;\boldsymbol{x}_0)}\frac{\mathrm{d}v(t;\boldsymbol{x}_0)}{\mathrm{d}t}, \tag{D8a}$$

$$\gamma'(t;\boldsymbol{x}_0)=\tilde{\epsilon}_{12}(t;\boldsymbol{x}_0)+\tilde{\epsilon}_{21}(t;\boldsymbol{x}_0), \tag{D8b}$$

with

$$\tilde{\boldsymbol{\epsilon}}(t;\boldsymbol{x}_0)=\boldsymbol{A}(t;\boldsymbol{x}_0)^{\top}\boldsymbol{\epsilon}(t;\boldsymbol{x}_0)\boldsymbol{A}(t;\boldsymbol{x}_0). \tag{D9}$$

Now adding diffusion to this picture following (Dentz *et al.* 2018), the Lagrangian description of a solute particle undergoing advection and diffusion is given by

$$\mathrm{d}\boldsymbol{x}(t;\boldsymbol{x}_0)=\boldsymbol{u}[\boldsymbol{x}(t;\boldsymbol{x}_0)]\mathrm{d}t+\sqrt{2D}\mathrm{d}\boldsymbol{W}_t, \tag{D10}$$

whose distance to the streamline is

$$z(t;\boldsymbol{x}_0,\boldsymbol{x}_0)=\boldsymbol{x}(t;\boldsymbol{x}_0)-\boldsymbol{x}(t;\boldsymbol{x}_0), \tag{D11}$$

and evolves according to

$$\mathrm{d}z(t;\boldsymbol{x}_0,\boldsymbol{x}_0)=\boldsymbol{\epsilon}(t;\boldsymbol{x}_0)z(t;\boldsymbol{x}_0,\boldsymbol{x}_0)\mathrm{d}t+\sqrt{2D}\mathrm{d}\boldsymbol{W}_t. \tag{D12}$$

Upon rotating to the streamline coordinate system through $z'(t;\boldsymbol{x}_0,\boldsymbol{x}_0)=\boldsymbol{A}(t;\boldsymbol{x}_0)^{\top}z(t;\boldsymbol{x}_0,\boldsymbol{x}_0)$, we arrive at

$$\mathrm{d}z'(t;\boldsymbol{x}_0,\boldsymbol{x}_0)=\boldsymbol{\epsilon}'(t;\boldsymbol{x}_0)z'(t;\boldsymbol{x}_0,\boldsymbol{x}_0)\mathrm{d}t+\sqrt{2D}\mathrm{d}\boldsymbol{W}_t, \tag{D13}$$

where we have used the fact that, due to isotropy, the noise term is statistically unaffected by rotation. That is, the components of the Wiener process $\boldsymbol{W}_t$ have the same statistical properties in the rotated coordinate system as in the original one, and we retain the same

https://doi.org/10.1017/jfm.2025.11092 Published online by Cambridge University Press

symbol for simplicity. We note in particular that in the streamline coordinate system the second component describes an Ornstein–Uhlenbeck process (Dentz *et al.* 2018) with time-dependent drift, by virtue of the upper-triangular form of the velocity gradient tensor (D7). The description of the Ornstein–Uhlenbeck process with constant drift in hyperbolic form was presented in Domínguez-Vázquez *et al.* (2024*b*), here summarised in Appendix C. Equation (3.6) is the FPE associated with (D13). Note that we have dropped the primes in the main text for readability.

Appendix E. Forward and backward maps

To derive forward and backward maps for the support of the joint PDF $f_{\boldsymbol{X}\boldsymbol{\Xi}}$, consider the separation between a diffusive particle and a streamline, given by $z(t; \boldsymbol{x}_0, \boldsymbol{x}_0)$ in the streamline frame. We set $t_0 = 0$ for simplicity. This is obtained by rotating the laboratory-frame definition in (D11), i.e.

$$z(t; \boldsymbol{x}_0, \boldsymbol{x}_0) = \boldsymbol{A}(t; \boldsymbol{x}_0)^\top \left[\boldsymbol{x}(t; \boldsymbol{x}_0) - \boldsymbol{x}(t; \boldsymbol{x}_0)\right]. \tag{E1}$$

Note that we have dropped the prime denoting the streamline frame on z. The initial separation between the diffusive particle and the streamline is given by

$$z_0 = z(0; \boldsymbol{x}_0, \boldsymbol{x}_0) = \boldsymbol{A}(0; \boldsymbol{x}_0)^\top \left[\boldsymbol{x}_0 - \boldsymbol{x}_0\right]. \tag{E2}$$

To switch to the hyperbolic description, we substitute the characteristic $\hat{\boldsymbol{x}}(t; \boldsymbol{\xi}, \boldsymbol{x}_0, \boldsymbol{x}_0)$ for the path $\boldsymbol{x}(t; \boldsymbol{x}_0)$ of the diffusive particle and $\hat{z}(t; \boldsymbol{\xi}, \boldsymbol{x}_0, \boldsymbol{x}_0)$ for the separation $z(t; \boldsymbol{x}_0, \boldsymbol{x}_0)$ in (E1). Note that these characteristics depend in general on an additional parameter $\boldsymbol{x}_0$, because they are parameterised in terms of their starting point $\boldsymbol{x}_0$ and are to be found in terms of a reference streamline starting at a possibly different point $\boldsymbol{x}_0$. Using (3.15) for $\hat{z}$, we find that

$$\boldsymbol{B}(t; \boldsymbol{x}_0) z_0 + \boldsymbol{\zeta}(t; \boldsymbol{x}_0)^\top \boldsymbol{\xi} = \boldsymbol{A}(t; \boldsymbol{x}_0)^\top \big[\hat{\boldsymbol{x}}(t; \boldsymbol{\xi}, \boldsymbol{x}_0) - \boldsymbol{x}(t; \boldsymbol{x}_0)\big], \tag{E3}$$

where $\boldsymbol{B}(t; \boldsymbol{x}_0)$ and $\boldsymbol{\zeta}(t; \boldsymbol{x}_0)$ are given by (3.16) and (3.10) for a given initial location $\boldsymbol{x}_0$. Using (E2) for z_0 and solving for $\hat{\boldsymbol{x}}$, the forward map is

$$\begin{aligned} \hat{\boldsymbol{x}}(t; \boldsymbol{\xi}, \boldsymbol{x}_0, \boldsymbol{x}_0) = \boldsymbol{x}(t; \boldsymbol{x}_0) \\ + \boldsymbol{A}(t; \boldsymbol{x}_0)\big[\boldsymbol{B}(t; \boldsymbol{x}_0)\boldsymbol{A}(0; \boldsymbol{x}_0)^\top (\boldsymbol{x}_0 - \boldsymbol{x}_0) + \boldsymbol{\zeta}(t; \boldsymbol{x}_0)^\top \boldsymbol{\xi}\big]. \end{aligned} \tag{E4}$$

Note that this depends on $\boldsymbol{x}_0$ only through the initial distance $\boldsymbol{x}_0 - \boldsymbol{x}_0$ to the reference streamline. If the diffusive particle lies at the reference streamline at the initial time, i.e. $\boldsymbol{x}_0 = \boldsymbol{x}_0$, relation (E4) leads to (4.1) for the usual characteristics $\hat{\boldsymbol{x}}(t; \tilde{\boldsymbol{\xi}}, \boldsymbol{x}_0)$.

We now wish to obtain the backward map $\hat{\boldsymbol{x}}_0(\boldsymbol{\xi}, \boldsymbol{x}, t)$ associated with a point in space $\boldsymbol{x} = \hat{\boldsymbol{x}}(t; \tilde{\boldsymbol{\xi}}, \boldsymbol{x}_0)$. We combine (3.18) with (E2) to write

$$\boldsymbol{A}(0; \boldsymbol{x}_0)^\top \big[\hat{\boldsymbol{x}}_0[\boldsymbol{\xi}, \hat{\boldsymbol{x}}(t; \tilde{\boldsymbol{\xi}}, \boldsymbol{x}_0), t] - \boldsymbol{x}_0\big] = \boldsymbol{B}(t; \boldsymbol{x}_0)^{-1} \big[\hat{z}(t; \tilde{\boldsymbol{\xi}}, \boldsymbol{x}_0, \boldsymbol{x}_0) - \boldsymbol{\zeta}(t; \boldsymbol{x}_0)^\top \boldsymbol{\xi}\big], \tag{E5}$$

from which

$$\hat{\boldsymbol{x}}_0[\boldsymbol{\xi}, \hat{\boldsymbol{x}}(t; \tilde{\boldsymbol{\xi}}, \boldsymbol{x}_0), t] = \boldsymbol{x}_0 + \boldsymbol{A}(0; \boldsymbol{x}_0)\boldsymbol{B}(t; \boldsymbol{x}_0)^{-1} [\hat{z}(t; \tilde{\boldsymbol{\xi}}, \boldsymbol{x}_0, \boldsymbol{x}_0) - \boldsymbol{\zeta}(t; \boldsymbol{x}_0)^\top \boldsymbol{\xi}]. \tag{E6}$$

From (3.15), together with $z_0 = \boldsymbol{0}$ for $\boldsymbol{x}_0 = \boldsymbol{x}_0$, see (E2), we have

$$\hat{z}(t; \tilde{\boldsymbol{\xi}}, \boldsymbol{x}_0, \boldsymbol{x}_0) = \boldsymbol{\zeta}(t; \boldsymbol{x}_0)^\top \tilde{\boldsymbol{\xi}}. \tag{E7}$$

Substituting in (E6) yields (4.3).

Finally, we are interested in computing the backward map $\hat{\boldsymbol{x}}_0(\boldsymbol{\xi}, \boldsymbol{x}, t)$ for an arbitrary point $\boldsymbol{x}$ in space at time t. To do so, we make use of the backward flow map (4.5),

https://doi.org/10.1017/jfm.2025.11092 Published online by Cambridge University Press

which involves solving (D1) backwards in time to find the initial point $\hat{\boldsymbol{x}}_0(\boldsymbol{x}, t)$ along a streamline. Then, combining (3.18) and (E2) leads to

$$-\boldsymbol{B}[t; \hat{\boldsymbol{x}}_0(\boldsymbol{x}, t)]^{-1}\boldsymbol{\zeta}[t; \hat{\boldsymbol{x}}_0(\boldsymbol{x}, t)]^{\top}\boldsymbol{\xi} = \boldsymbol{A}[0; \hat{\boldsymbol{x}}_0(\boldsymbol{x}, t)]^{\top}\left[\hat{\boldsymbol{x}}_0(\boldsymbol{\xi}, \boldsymbol{x}, t) - \hat{\boldsymbol{x}}_0(\boldsymbol{x}, t)\right], \quad \text{(E8)}$$

where in (3.18) we take $\boldsymbol{z} = \boldsymbol{0}$, i.e. the streamline and the diffusive particle coincide at time t. Solving for $\hat{\boldsymbol{x}}_0$ leads to (4.6).

References

Anderson, B.D.O. 1982 Reverse-time diffusion equation models. *Stoch. Proc. Appl.* **12** (3), 313–326.

Aquino, T. 2024 Coupled nonlinear surface reactions in random walk particle tracking. *Adv. Water Resour.* **185**, 104656.

Aquino, T. & Bolster, D. 2017 Localized point mixing rate potential in heterogeneous velocity fields. *Transport Porous Med.* **119**, 391–402.

Aquino, T., Le Borgne, T. & Heyman, J. 2023 Fluid–solid reaction in porous media as a chaotic restart process. *Phys. Rev. Lett.* **130** (26), 264001.

Balkovsky, E. & Fouxon, A. 1999 Universal long-time properties of Lagrangian statistics in the Batchelor regime and their application to the passive scalar problem. *Phys. Rev. E* **60** (4), 4164.

Bear, J. 1972 *Dynamics of Fluids in Porous Media*. American Elsevier Publishing Company, Inc.

Benson, D.A., Aquino, T., Bolster, D., Engdahl, N., Henri, C.V. & Fernandez-Garcia, D. 2017 A comparison of Eulerian and Lagrangian transport and non-linear reaction algorithms. *Adv. Water Resour.* **99**, 15–37.

Benson, D.A., Bolster, D., Pankavich, S. & Schmidt, M.J. 2021 Nonparametric, data-based kernel interpolation for particle-tracking simulations and kernel density estimation. *Adv. Water Resour.* **152**, 103889.

Bolster, D., Dentz, M. & Le Borgne, T. 2011 Hypermixing in linear shear flow. *Water Resour. Res.* **47** (9), W09602.

Bonazzi, A., Dentz, M. & de Barros, F.P.J. 2023*a* Mixing in multidimensional porous media: a numerical study of the effects of source configuration and heterogeneity. *Transport Porous Med.* **146** (1), 369–393.

Bonazzi, A., Jha, B. & de Barros, F.P.J. 2023*b* Influence of initial plume shape on miscible porous media flows under density and viscosity contrasts. *J. Fluid Mech.* **972**, A19.

Cramér, H. 1946 *Mathematical methods of statistics*. In *Princeton Mathematical Series*, vol. 9, Princeton University Press.

Dagan, G. 1984 Solute transport in heterogeneous porous formations. *J. Fluid Mech.* **145**, 151–177.

De Barros, F.P.J., Dentz, M., Koch, J. & Nowak, W. 2012 Flow topology and scalar mixing in spatially heterogeneous flow fields. *Geophys. Res. Lett.* **39** (8), L08404.

Demuren, A.O. & Rodi, W. 1986 Calculation of flow and pollutant dispersion in meandering channels. *J. Fluid Mech.* **172**, 63–92.

Dentz, M. & de Barros, F.P.J. 2015 Mixing-scale dependent dispersion for transport in heterogeneous flows. *J. Fluid Mech.* **777**, 178–195.

Dentz, M., de Barros, F.P.J., Le Borgne, T. & Lester, D.R. 2018 Evolution of solute blobs in heterogeneous porous media. *J. Fluid Mech.* **853**, 621–646.

Dentz, M., Hidalgo, J.J. & Lester, D. 2023 Mixing in porous media: concepts and approaches across scales. *Transport Porous Med.* **146** (1), 5–53.

Dentz, M., Le Borgne, T., Englert, A. & Bijeljic, B. 2011 Mixing, spreading and reaction in heterogeneous media: a brief review. *J. Contam. Hydrol.* **120**, 1–17.

Dentz, M., Lester, D.R., Le Borgne, T. & De Barros, F.P.J. 2016 Coupled continuous-time random walks for fluid stretching in two-dimensional heterogeneous media. *Phys. Rev. E* **94** (6), 061102.

Dimotakis, P.E. 2005 Turbulent mixing. *Annu. Rev. Fluid Mech.* **37** (1), 329–356.

Domínguez-Vázquez, D., Castiblanco-Ballesteros, S.A., Jacobs, G.B. & Tartakovsky, D.M. 2024*a* High-order Lagrangian algorithms for Liouville models of particle-laden flows. *J. Comput. Phys.* **515**, 113281.

Domínguez-Vázquez, D., Jacobs, G.B. & Tartakovsky, D.M. 2021 Lagrangian models of particle-laden flows with stochastic forcing: Monte Carlo, moment equations, and method of distributions analyses. *Phys. Fluids* **33** (3), 033326.

Domínguez-Vázquez, D., Jacobs, G.B. & Tartakovsky, D.M. 2024*b* Liouville models of particle-laden flow. *Phys. Fluids* **36** (6), 063303.

https://doi.org/10.1017/jfm.2025.11092 Published online by Cambridge University Press

EGAN, B.A. & MAHONEY, J.R. 1972 Numerical modeling of advection and diffusion of urban area source pollutants. *J. Appl. Meteorol. Clim.* **11** (2), 312–322.

FERNÀNDEZ-GARCIA, D. & SÁNCHEZ-VILA, X. 2011 Optimal reconstruction of concentrations, gradients and reaction rates from particle distributions. *J. Contam. Hydrol.* **120**, 99–114.

GOTTLIEB, S. & SHU, C.W. 1998 Total variation diminishing Runge–Kutta schemes. *Math. Comput.* **67** (221), 73–85.

GUERRERO-HURTADO, M., GARCIA-VILLALBA, M., GONZALO, A., MARTINEZ-LEGAZPI, P., KAHN, A.M., MCVEIGH, E., BERMEJO, J., DEL ALAMO, J.C. & FLORES, O. 2023 Efficient multi-fidelity computation of blood coagulation under flow. *PLOS Comput. Biol.* **19** (10), e1011583.

HALLER, G. 2015 Lagrangian coherent structures. *Annu. Rev. Fluid Mech.* **47**, 137–162.

HALLER, G. & YUAN, G. 2000 Lagrangian coherent structures and mixing in two-dimensional turbulence. *Phys. D: Nonlinear Phenomena* **147** (3–4), 352–370.

HALMOS, P.R. 1950 Haar measure. In *Measure Theory*, pp. 250–265. Springer.

HEYMAN, J., LESTER, D.R., TURUBAN, R., MÉHEUST, Y. & LE BORGNE, T. 2020 Stretching and folding sustain microscale chemical gradients in porous media. *Proc. Natl Acad. Sci. USA* **117** (24), 13359–13365.

HEYMAN, J., VILLERMAUX, E., DAVY, P. & LE BORGNE, T. 2024 Mixing as a correlated aggregation process. *J. Fluid Mech.* **992**, A6.

KÁROLYI, G., SCHEURING, I. & CZÁRÁN, T. 2002 Metabolic network dynamics in open chaotic flow. *Chaos: Interdiscip. J. Nonlinear Sci.* **12** (2), 460–469.

KINZELBACH, W. & UFFINK, G. 1991 The random walk method and extensions in groundwater modelling. In *Transport Processes in Porous Media* (eds. J. Bear & M.Y. Corapcioglu, vol. 202, pp. 761–787, Springer.

KLOEDEN, P. & PLATEN, E. 1992 *Numerical Solution of Stochastic Differential Equations*. Springer.

LE BORGNE, T., DENTZ, M. & VILLERMAUX, E. 2015 The lamellar description of mixing in porous media. *J. Fluid Mech.* **770**, 458–498.

LESTER, D.R., DENTZ, M., BANDOPADHYAY, A. & LE BORGNE, T. 2021 The Lagrangian kinematics of three-dimensional Darcy flow. *J. Fluid Mech.* **918**, A27.

LESTER, D.R., DENTZ, M., BANDOPADHYAY, A. & LE BORGNE, T. 2022 Fluid deformation in isotropic Darcy flow. *J. Fluid Mech.* **945**, A18.

LESTER, D.R., DENTZ, M., LE BORGNE, T. & DE BARROS, F.P.J. 2018 Fluid deformation in random steady three-dimensional flow. *J. Fluid Mech.* **855**, 770–803.

LESTER, D.R., METCALFE, G. & TREFRY, M.G. 2013 Is chaotic advection inherent to porous media flow? *Phys. Rev. Lett.* **111** (17), 174101.

LV, Y. & IHME, M. 2014 Discontinuous Galerkin method for multicomponent chemically reacting flows and combustion. *J. Comput. Phys.* **270**, 105–137.

MARTÍNEZ-RUIZ, D., MEUNIER, P., FAVIER, B., DUCHEMIN, L. & VILLERMAUX, E. 2018 The diffusive sheet method for scalar mixing. *J. Fluid Mech.* **837**, 230–257.

MARUYAMA, G. 1955 Continuous Markov processes and stochastic equations. *Rendiconti del Circolo Matematico di Palermo* **4** (1), 48–90.

MEUNIER, P. & VILLERMAUX, E. 2003 How vortices mix. *J. Fluid Mech.* **476**, 213–222.

MEUNIER, P. & VILLERMAUX, E. 2010 The diffusive strip method for scalar mixing in two dimensions. *J. Fluid Mech.* **662**, 134–172.

MEUNIER, P. & VILLERMAUX, E. 2022 The diffuselet concept for scalar mixing. *J. Fluid Mech.* **951**, A33.

MONSON, E. & KOPELMAN, R. 2000 Observation of laser speckle effects and nonclassical kinetics in an elementary chemical reaction. *Phys. Rev. Lett.* **85** (3), 666.

MOYAL, J.E. 1949 Stochastic processes and statistical physics. *J. R. Statist. Soc. Series B (Methodological)* **11** (2), 150–210.

NOETINGER, B., ROUBINET, D., RUSSIAN, A., LE BORGNE, T., DELAY, F., DENTZ, M., DE DREUZY, J.R. & GOUZE, P. 2016 Random walk methods for modeling hydrodynamic transport in porous and fractured media from pore to reservoir scale. *Transport Porous Med.* **115**, 345–385.

OTTINO, J.M. 1990 Mixing, chaotic advection, and turbulence. *Annu. Rev. Fluid Mech.* **22** (1), 207–254.

OWEN, D.B. 1980 A table of normal integrals. *Commun. Stat. Simulat.* **9** (4), 389–419.

PASTER, A., BOLSTER, D. & BENSON, D.A. 2014 Connecting the dots: semi-analytical and random walk numerical solutions of the diffusion-reaction equation with stochastic initial conditions. *J. Comput. Phys.* **263**, 91–112.

PEDRETTI, D. & FERNÀNDEZ-GARCIA, D. 2013 An automatic locally-adaptive method to estimate heavily-tailed breakthrough curves from particle distributions. *Adv. Water Resour.* **59**, 52–65.

PIROZZOLI, S., BERNARDINI, M. & ORLANDI, P. 2016 Passive scalars in turbulent channel flow at high Reynolds number. *J. Fluid Mech.* **788**, 614–639.

https://doi.org/10.1017/jfm.2025.11092 Published online by Cambridge University Press

POPE, S.B. 1985 PDF methods for turbulent reactive flows. *Prog. Energ. Combust.* **11** (2), 119–192.
POPE, S.B. 1987 Turbulent premixed flames. *Annu. Rev. Fluid Mech.* **19** (1), 237–270.
PUSHENKO, V., SCOLLO, S., MEUNIER, P., VILLERMAUX, E. & SCHUMACHER, J. 2025 Diffuselet method for three-dimensional turbulent mixing of a cloudy air filament. *Phys. Rev. Fluids* **10** (7), 074503.
PUYGUIRAUD, A., PEREZ, L.J., HIDALGO, J.J. & DENTZ, M. 2020 Effective dispersion coefficients for the upscaling of pore-scale mixing and reaction. *Adv. Water Resour.* **146**, 103782.
RANZ, W.E. 1979 Applications of a stretch model to mixing, diffusion, and reaction in laminar and turbulent flows. *AIChE J.* **25** (1), 41–47.
RISKEN, H. 1996 *The Fokker-Planck Equation*. Springer.
RIZZO, C.B., NAKANO, A. & DE BARROS, F.P.J. 2019 Par2: parallel random walk particle tracking method for solute transport in porous media. *Comput. Phys. Commun.* **239**, 265–271.
SALAMON, P., FERNÀNDEZ-GARCIA, D. & GÓMEZ-HERNÁNDEZ, J.J. 2006 A review and numerical assessment of the random walk particle tracking method. *J. Contam. Hydrol.* **87** (3-4), 277–305.
SEN, S., SINGH, P., HEYMAN, J., LE BORGNE, T. & BANDOPADHYAY, A. 2020 The impact of stretching-enhanced mixing and coalescence on reactivity in mixing-limited reactive flows. *Phys. Fluids* **32** (10), 106602.
SHADDEN, S.C., LEKIEN, F. & MARSDEN, J.E. 2005 Definition and properties of Lagrangian coherent structures from finite-time Lyapunov exponents in two-dimensional aperiodic flows. *Phys. D: Nonlinear Phenomena* **212** (3-4), 271–304.
SHU, C.W. 2020 Essentially non-oscillatory and weighted essentially non-oscillatory schemes. *Acta Numer.* **29**, 701–762.
SOLE-MARI, G., BOLSTER, D., FERNÀNDEZ-GARCIA, D. & SANCHEZ-VILA, X. 2019 Particle density estimation with grid-projected and boundary-corrected adaptive kernels. *Adv. Water Resour.* **131**, 103382.
SOONG, T.T. 1973 *Random differential equations in science and engineering*. In *Mathematics in Science and Engineering*, 1st edn, vol. 103. Elsevier Science & Technology.
SOUZY, M., ZAIER, I., LHUISSIER, H., LE BORGNE, T. & METZGER, B. 2018 Mixing lamellae in a shear flow. *J. Fluid Mech.* **838**, R3.
SUAREZ, J.P. & JACOBS, G.B. 2017 Regularization of singularities in the weighted summation of Dirac–delta functions for the spectral solution of hyperbolic conservation laws. *J. Sci. Comput.* **72** (3), 1080–1092.
SUAREZ, J.P., JACOBS, G.B. & DON, W.S. 2014 A high–order Dirac–delta regularization with optimal scaling in the spectral solution of one–dimensional singular hyperbolic conservation laws. *SIAM J. Sci. Comput.* **36** (4), A1831–A1849.
TARTAKOVSKY, A.M., TARTAKOVSKY, G.D. & SCHEIBE, T.D. 2009 Effects of incomplete mixing on multicomponent reactive transport. *Adv. Water Resour.* **32** (11), 1674–1679.
TARTAKOVSKY, D.M. 2013 Assessment and management of risk in subsurface hydrology: a review and perspective. *Adv. Water Resour.* **51**, 247–260.
TARTAKOVSKY, D.M. & GREMAUD, P.A. 2015 Method of distributions for uncertainty quantification. In *Handbook of Uncertainty Quantification* (eds. R. Ghanem, D. Higdon & H. Owhadi), pp. 763–783, Springer.
TURUBAN, R., LESTER, D.R., HEYMAN, J., LE BORGNE, T. & MÉHEUST, Y. 2019 Chaotic mixing in crystalline granular media. *J. Fluid Mech.* **871**, 562–594.
TURUBAN, R., LESTER, D.R., LE BORGNE, T. & MÉHEUST, Y. 2018 Space-group symmetries generate chaotic fluid advection in crystalline granular media. *Phys. Rev. Lett.* **120** (2), 024501.
VALOCCHI, A.J., BOLSTER, D. & WERTH, C.J. 2019 Mixing-limited reactions in porous media. *Transport Porous Med.* **130**, 157–182.
VAN KAMPEN, N.G. 1992 *Stochastic Processes in Physics and Chemistry*, vol. 1. Elsevier.
VENTURI, D. & KARNIADAKIS, G.E. 2012 New evolution equations for the joint response-excitation probability density function of stochastic solutions to first-order nonlinear PDEs. *J. Comput. Phys.* **231** (21), 7450–7474.
VENTURI, D., TARTAKOVSKY, D.M., TARTAKOVSKY, A.M. & KARNIADAKIS, G.E. 2013 Exact PDF equations and closure approximations for advective-reactive transport. *J. Comput. Phys.* **243**, 323–343.
VILLERMAUX, E. 2019 Mixing versus stirring. *Annu. Rev. Fluid Mech.* **51** (1), 245–273.
WHITTAKER, E.T. 1943 Chance, freewill and necessity in the scientific conception of the universe. *Proc. Phys. Soc.* **55** (6), 459.
WINTER, H.H. 1982 Modelling of strain histories for memory integral fluids in steady axisymmetric flows. *J. Non-Newtonian Fluid Mech.* **10** (1-2), 157–167.
WISSINK, B.W., JACOBS, G.B., RYAN, J.K., DON, W.S. & VAN DER WEIDE, E.T.A. 2018 Shock regularization with smoothness-increasing accuracy-conserving Dirac-delta polynomial kernels. *J. Sci. Comput.* **77** (1), 579–596.

https://doi.org/10.1017/jfm.2025.11092 Published online by Cambridge University Press

WRIGHT, E.E., RICHTER, D.H. & BOLSTER, D. 2017 Effects of incomplete mixing on reactive transport in flows through heterogeneous porous media. *Phys. Rev. Fluids* **2** (11), 114501.

ZASLAVSKY, G.M. 2002 Chaos, fractional kinetics, and anomalous transport. *Phys. Rep.* **371** (6), 461–580.

ZHOU, L. & HANSEN, S.K. 2022 Directly generating spatially periodic, heterogeneous groundwater flow fields: a finite volume approach. *Water Resour. Res.* **58** (8), e2022WR032015.

ZHOU, L. & HANSEN, S.K. 2024 Upscaling transport in heterogeneous media featuring local-scale dispersion: flow channeling, macro-retardation and parameter prediction. *Adv. Water Resour.* **193**, 104830.

https://doi.org/10.1017/jfm.2025.11092 Published online by Cambridge University Press